Supplementary Information (SI) for Journal of Materials Chemistry A.

Supplementary Information

Factors in the Utilization of Corrosive Ruthenium in the Oxygen Evolution Electrode of Polymer Electrolyte Membrane Water Electrolysis

Suji Lee[ab], Chaeyeon Yang[ab], Jihyun Choi[ab], Jong Hyun Jang[ad], Haneul Jin*[c], Yung-Eun Sung*[b], and Hyun S. Park*[ad]

[a] *Center for Hydrogen·Fuel Cell Research, Korea Institute of Science and Technology (KIST), Seoul 02792, Republic of Korea. E-mail: hspark@kist.re.kr*

[b] *School of Chemical and Biological Engineering, Seoul National University, Seoul 08826, Republic of Korea. E-mail: ysung@snu.ac.kr*

[c] *Department of Energy and Materials Engineering, Dongguk University, Seoul 04620, Republic of Korea. E-mail: hjin1@dongguk.edu*

[d] *Division of Energy & Environment Technology, KIST School, University of Science and Technology (UST), Seoul 02792, Republic of Korea*

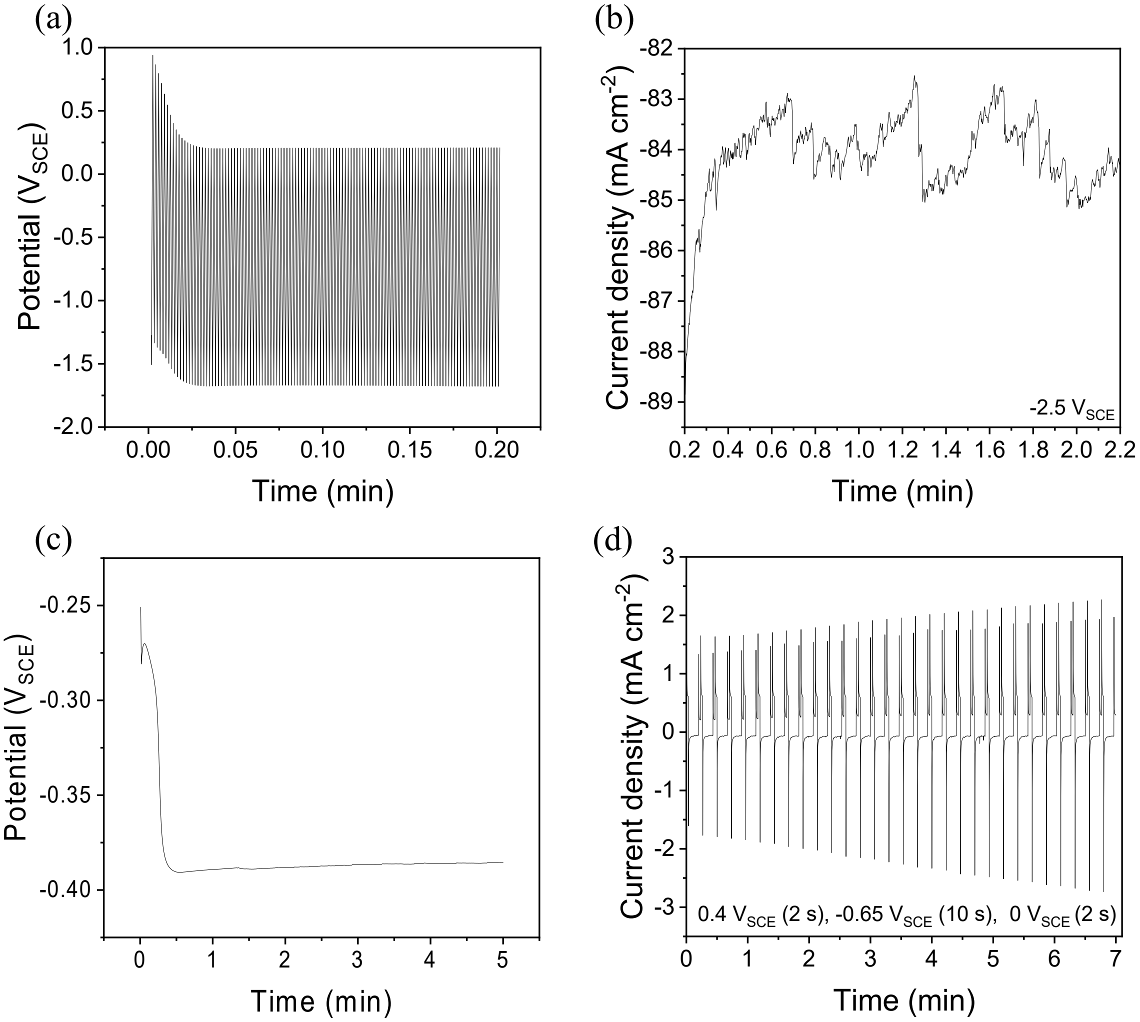

Fig. S1 CP and CA curves of Ru@Ir and Pt@Ir during electrodeposition. (a) CP curve of pre-cycling before Ru deposition, (b) CA curve of Ru 2 min (Ru 47 μg cm^{-2}), (c) CP curve of Pt deposition, and (d) CA curve of Ir deposition.

The reductive electrodeposition method utilizes protons adsorbed onto metals—such as Pt, Ru, and Pd—to regulate the deposition of the target metal. Therefore, in the present study, the deposition on bare Ti-PTL was not readily controlled because it was an ineffective H-adsorber in the absence of Ru or Pt; hence, pulse deposition ensured that the precious Ir catalyst was exclusively placed on the conductive Pt or Ru layers coated onto the Ti-PTL. The extent of Ir deposition was manipulated by controlling the pulse number. The anodes in which Ir was deposited on Ru/Ti-PTL and Pt/Ti-PTL are denoted Ru@Ir and Pt@Ir, respectively, herein. Bare Ti-PTL was not considered for further analysis because it showed insignificant water electrolysis performance without the Ir catalyst.

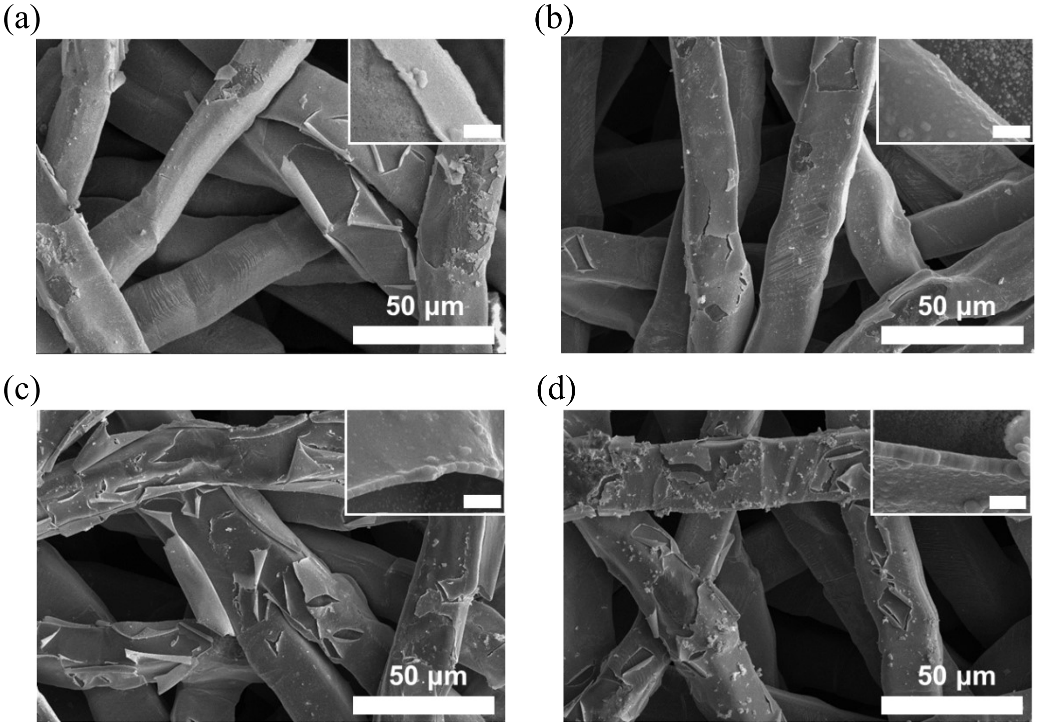

Fig. S2 SEM images of Ru electrodeposited on Ti-PTL (Ru/Ti-PTL) at varying deposition times. (a) 1 min (Ru 37 µg cm^{-2}), (b) 2 min (Ru 47 µg cm^{-2}), (c) 5 min (Ru 76 µg cm^{-2}), and (d) 10 min (Ru 113 µg cm^{-2}). (The inset images show the thickness of the Ru layer, with a scale bar in the top-right inset indicating 1 µm.)

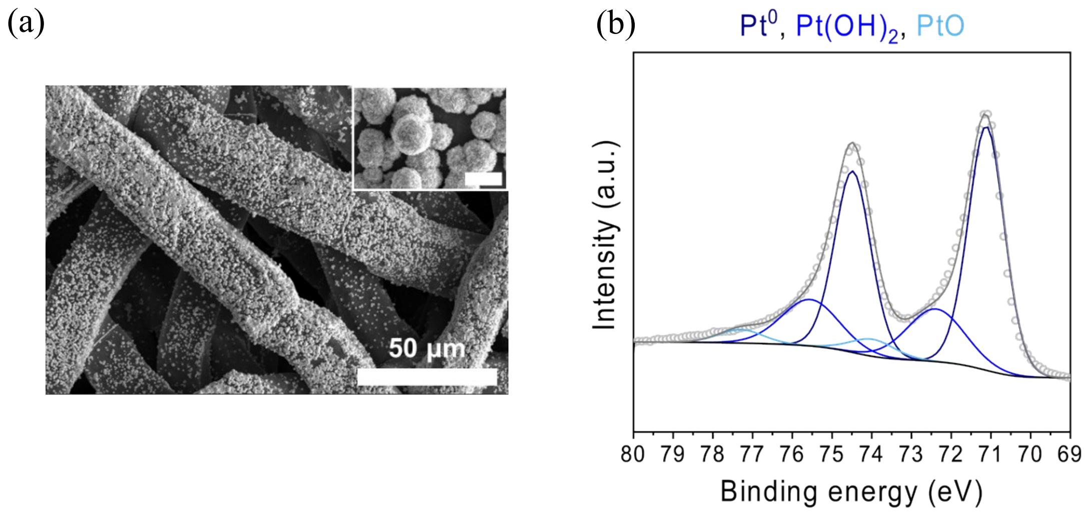

Fig. S3 (a) SEM image (scale bar in inset image on top-right: 1 μm), and (b) Pt 4f XPS spectra of electrodeposited Pt (Pt/Ti-PTL), with binding energies assigned to Pt^0 (71.2 and 74.5 eV), $Pt(OH)_2$ (72.3 and 75.5 eV), and PtO (74.0 and 77.3 eV).[1]

The noticeably different morphologies of the Ru/Ti-PTL implied the occurrence of different growth mechanisms (Fig. S2 and S3a). Ru interlayer presented a plain layer of uniform thickness over Ti-PTL surface implying there was rapid seeding and slow growth in the electrodeposition. On the other hands, the hemispherical Pt formed on the Ti-TPL with observable interfaces between the particles indicates that the deposition was proceeding with slower seeding with faster growth. The electrodeposited Pt in Pt@Ir exhibited a crystalline cubic structure with mostly metallic surfaces. Furthermore, the surface oxidation states of Pt mainly included those of metallic Pt (Pt^0, 67%), $Pt(OH)_2$ (24%), and PtO (9%), as indicated by the XPS spectra of Pt/Ti-PTL (Fig. S3b).

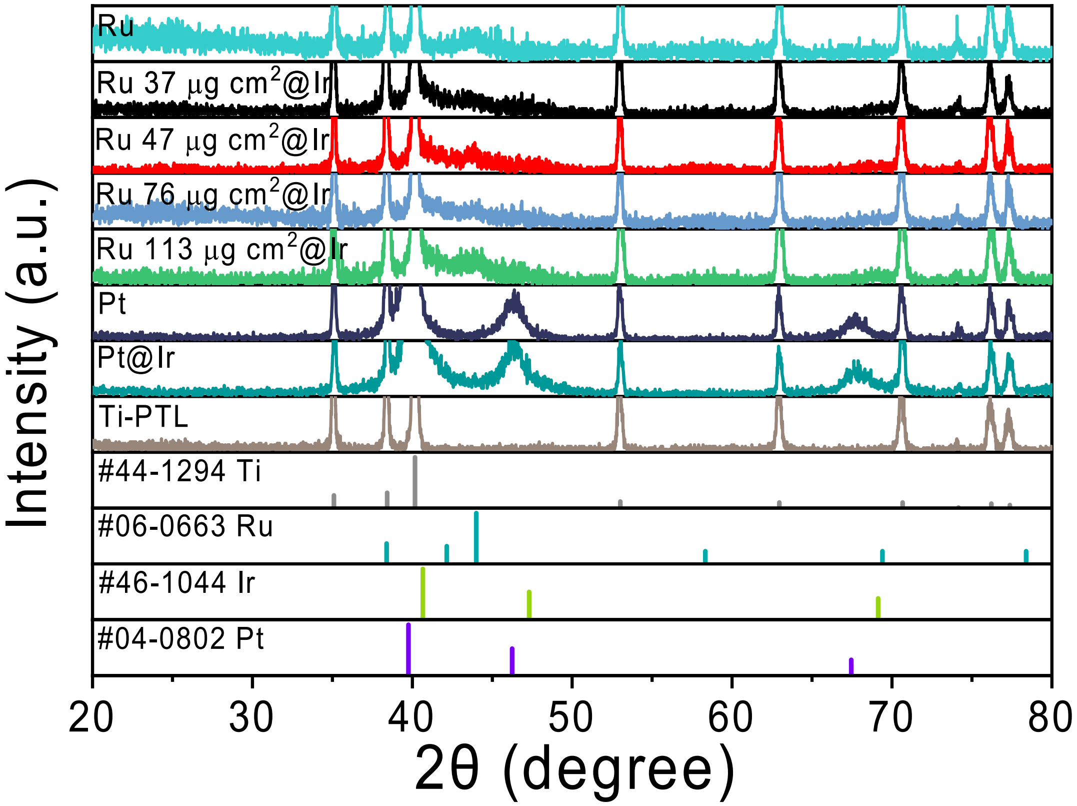

Fig. S4 XRD patterns of Ru, Ru 37 μg cm^{-2}@Ir, Ru 47 μg cm^{-2}@Ir, Ru 76 μg cm^{-2}@Ir, Ru 113 μg cm^{-2}@Ir, Pt, Pt@Ir, and Ti-PTL, along with reference.

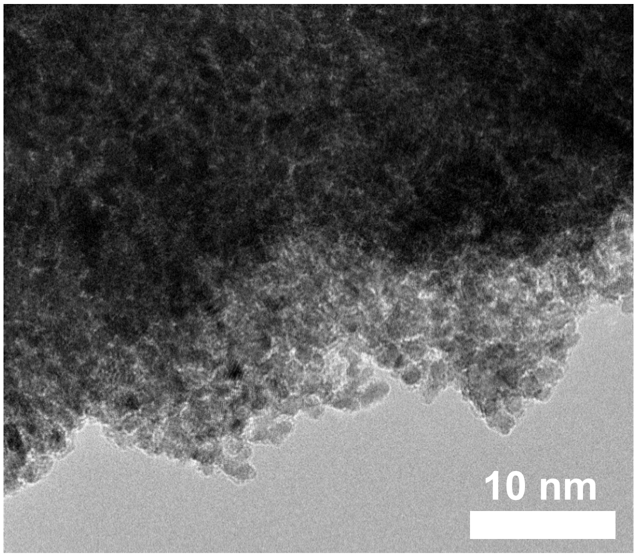

Fig. S5 TEM image of Ru 47 μg cm^{-2} specimen.

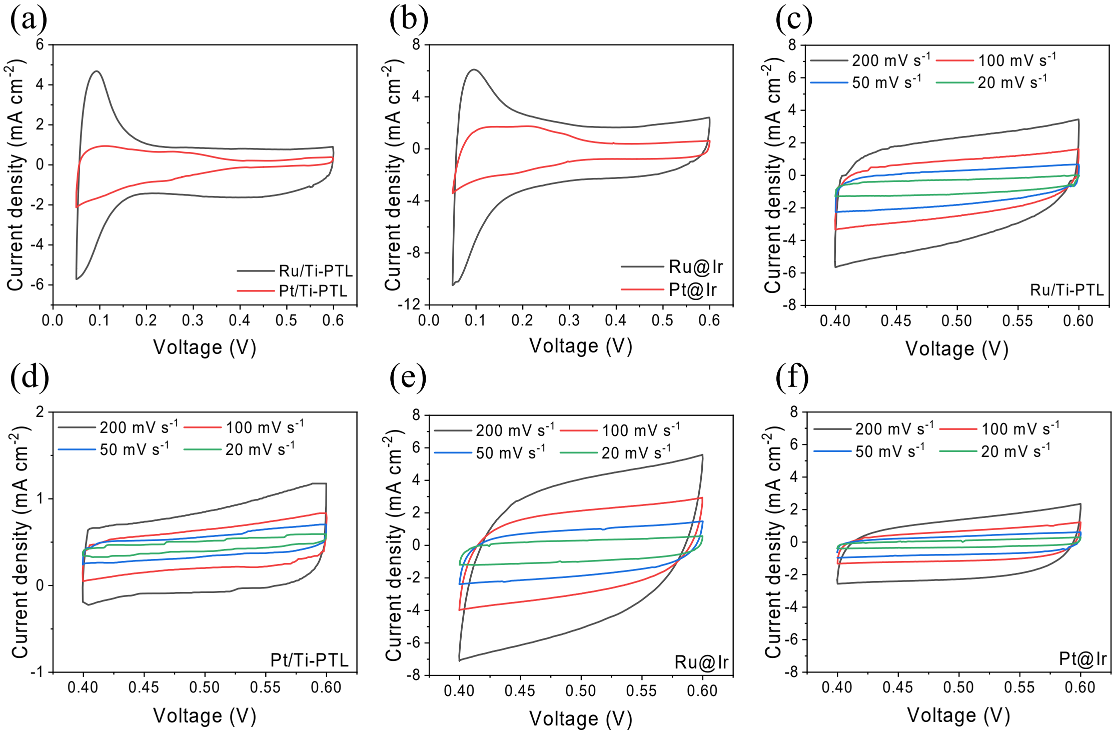

Fig. S6 CV curves of Ru/Ti-PTL, Pt/Ti-PTL, Ru@Ir, and Pt@Ir acquired to estimate electrochemically active surface area (ECSA) using hydrogen underpotential deposition (H_{upd}) and double-layer charging current (C_{dl}); CV curves for H_{upd} were obtained within the 0.05–0.60 V range (vs. pseudo RHE) at a scan rate of 50 mV s^{-1}, and those for C_{dl} were acquired in the 0.40–0.60 V range (vs. pseudo RHE) at scan rates ranging from 20 to 200 mV s^{-1}. CV curves of (a) Ru/Ti-PTL, Pt/Ti-PTL, (b) Ru@Ir, and Pt@Ir for H_{upd} analysis. CV curves of (c) Ru/Ti-PTL, (d) Pt/Ti PTL, (e) Ru@Ir, and (f) Pt@Ir for C_{dl} analysis.

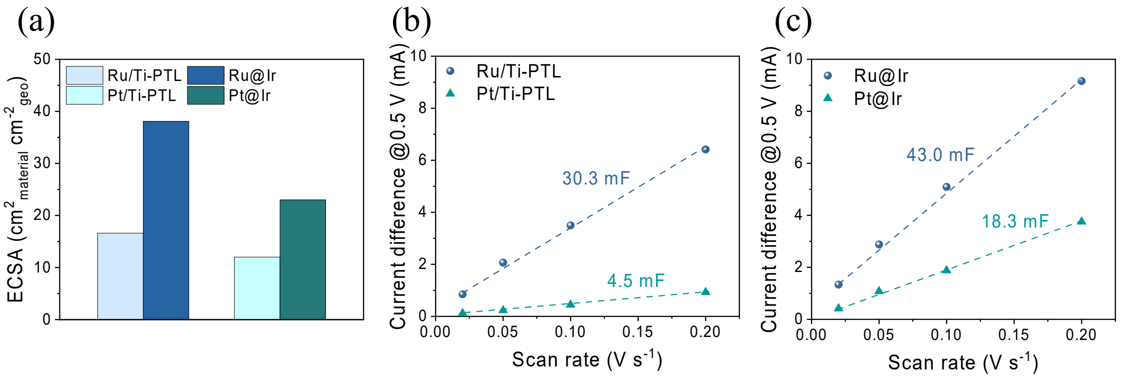

Fig. S7 Comparison of ECSA values derived from H_{upd} and C_{dl} before and after Ir deposition. (a) Bar graphs of ECSA obtained from H_{upd}, Linear plots of capacitive current against scan rate for (b) Ru/Ti-PTL, Pt/Ti PTL, (c) Ru@Ir, and Pt@Ir for C_{dl} analysis.

Although the Ru film on Ti-PTL showed a planar morphology without noticeable pores under microscopic images (Fig. S2), the small amorphous Ru particles in the Ru/Ti-PTL film delivered higher surfaces containing small features developed in the films. As a results, the ECSA by H_{upd} was about 17 and 12 $cm^2{}_{material}\ cm^{-2}{}_{geo}$, respectively, for Ru/Ti-PTL and Pt/Ti-PTL electrodes.

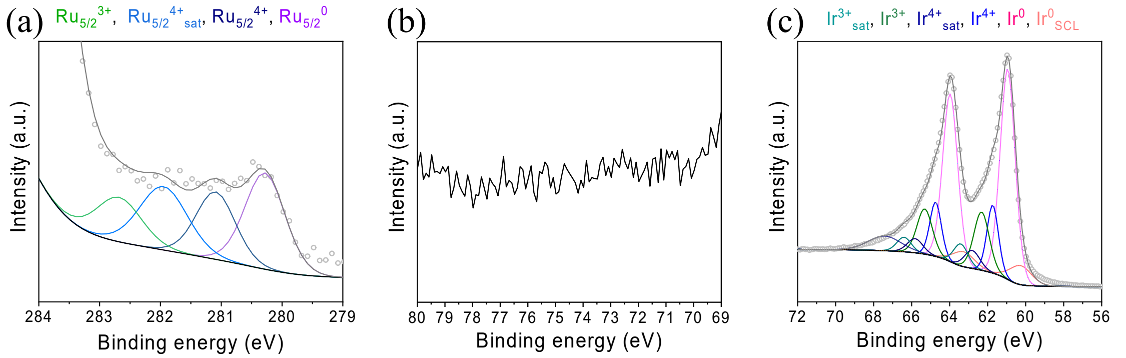

Fig. S8 XPS spectra of (a) Ru $3d_{5/2}$ in Ru@Ir, (b) Pt 4f in Pt@Ir, and (c) Ir 4f in Ru@Ir and Pt@Ir with fresh samples. Ru@Ir and Pt@Ir exhibited identical Ir 4f XPS spectra. The binding energies of the Ru $3d_{5/2}$ spectra were assigned to Ru^0 (280.2 eV), Ru^{3+} (282.3 eV), Ru^{4+} (281.1 eV), and Ru^{4+}_{sat} (282.7 eV),[2] whereas those of the Ir 4f spectra were ascribed to Ir^0_{SCL} (60.4 and 63.4 eV), Ir^0 (60.8 and 63.8 eV), Ir^{3+} (62.3 and 65.3 eV), Ir^{3+}_{sat} (63.33 and 66.3 eV), Ir^{4+} (61.7 and 64.7 eV), Ir^{4+}_{sat1} (62.8 and 65.8 eV), and Ir^{4+}_{sat2} (67.8 eV).[3] Owing to the lower intensity of Ru 3d than that of C–C (284.6 eV) in the XPS spectra, only Ru $3d_{5/2}$ was considered in this study.

The Ru and Pt interlayers in Ru@Ir and Pt@Ir, respectively, contained elements with mixed oxidation states, including metals, metal oxides, and hydroxides. The bulk crystal phase of Ru in Ru@Ir was ascribed to hexagonal Ru metal by XRD analysis (Fig. S4). However, the surface states of Ru in pristine Ru@Ir mainly included those of RuO_2 (49%), metallic Ru (Ru^0, 33%), and $Ru(OH)_3$ (18%), as determined by XPS spectra (Fig. S8a). The Ru surface was still noticeable in the Ru in Ru@Ir XPS spectra, whereas that of Pt was not discernible in the Pt in Pt@Ir XPS spectra (Fig. S8b). However, the surface oxidation state of electrodeposited Ir was unaffected by the interlayer. In both Ru@Ir and Pt@Ir, the electrodeposited Ir layer mainly comprised metallic Ir (Ir^0, 70%), IrO_2 (16%), and $Ir(OH)_3$ (14%) (Fig. S8c). The bulk crystal phase of the Ir film was not readily identified by XRD analysis, implying that the OER catalyst primarily contained amorphous nanoparticles (Fig. S4).

The electrodeposited Ru exhibited a less uniform structure compared to Pt (Fig. S2 and S3a). In this study, strategies to enhance the durability of Ru@Ir were investigated, and key factors influencing its long-term stability were identified. However, it is also anticipated that a more uniform deposition of the Ru layer could have further increased the electrochemically active surface area, thereby improving both the OER performance and the long-term stability of the material.

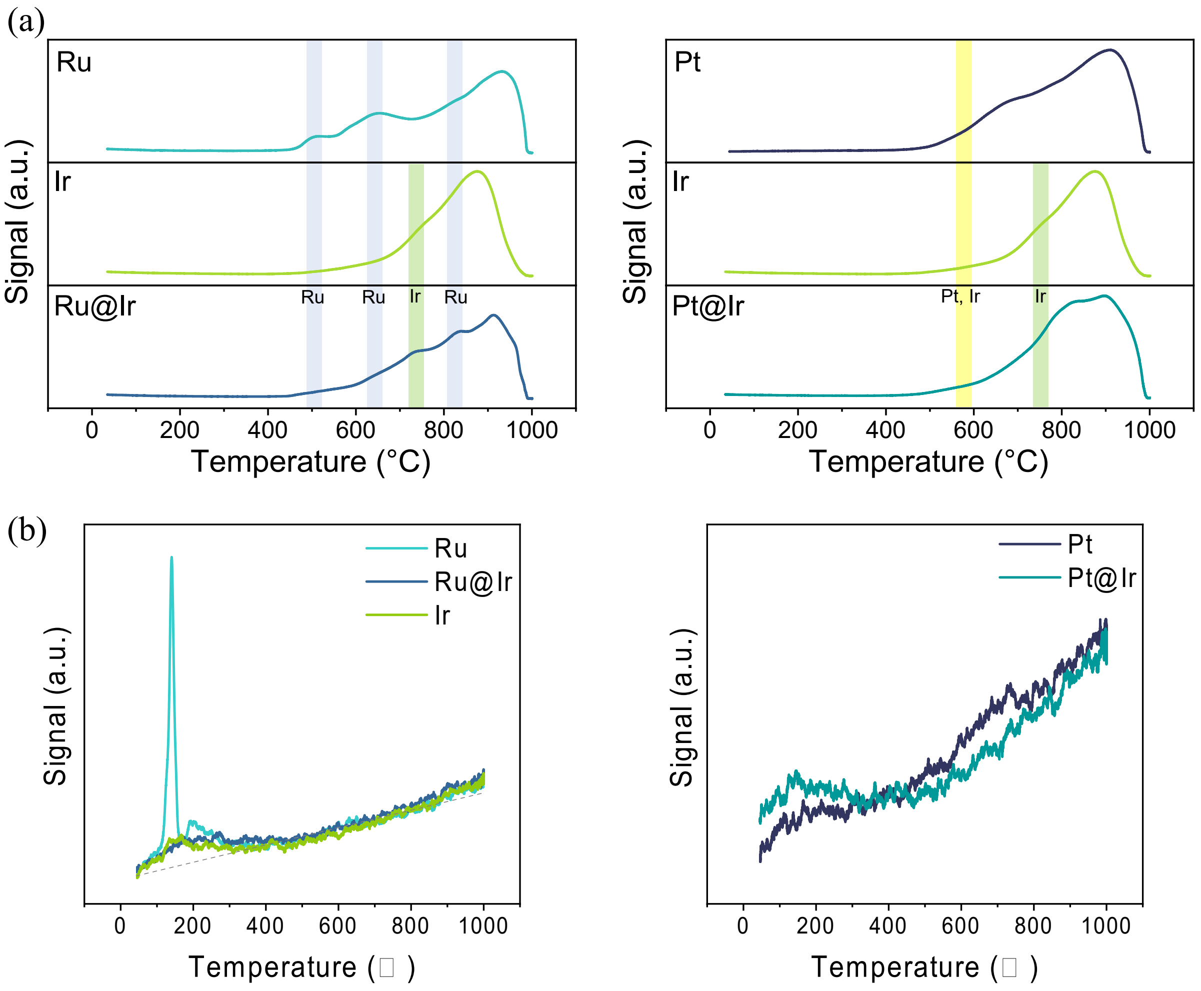

Fig. S9 (a) Temperature-programmed oxidation (TPO) and (b) temperature-programmed desorption (TPD) data of Ru, Ru@Ir, Ir, Pt, and Pt@Ir. TPD data indicates that all samples exhibit similar O_2 adsorption strengths, except oxophilic Ru.

In the TPO curves, the peak positions for Ru were observed at approximately 502, 645, 816, and 928°C, while those for Ir appeared at around 601, 738, and 873°C. The peak positions for Ru@Ir can largely be explained by a combination of peaks from both Ru and Ir, occurring at approximately 502, 645, 738, 816, and 913°C. This suggests that some Ru in Ru@Ir remained exposed on the surface, as confirmed by XPS spectra (Fig. S8a and c). For Pt and Pt@Ir, the peak positions for Pt were observed at approximately 601, 661, and 907°C, whereas those for Pt@Ir appeared at around 601, 738, 813, and 894°C. The absence of the 661 °C Pt peaks in Pt@Ir provides evidence that Pt was more effectively coated with Ir compared to Ru@Ir, while the peak at 601 °C can be from either Pt or Ir in Pt@Ir (Fig. S8b and c). The thermal oxidation of Ru and Pt observed in Ru@Ir and Pt@Ir during TPO analysis implies potential interactions of these metals with the electrolyte under water electrolysis conditions. Although the Ir layer in Ru@Ir and Pt@Ir largely mitigates such interactions, the results suggest that Ru and Pt remain susceptible to reactions with water or oxygen in the electrolyte. In this study, the electrochemical durability of Ru@Ir and Pt@Ir was investigated, with particular attention to the potential interactions between electrolyte components and the underlying Ru and Pt in the composite catalysts.

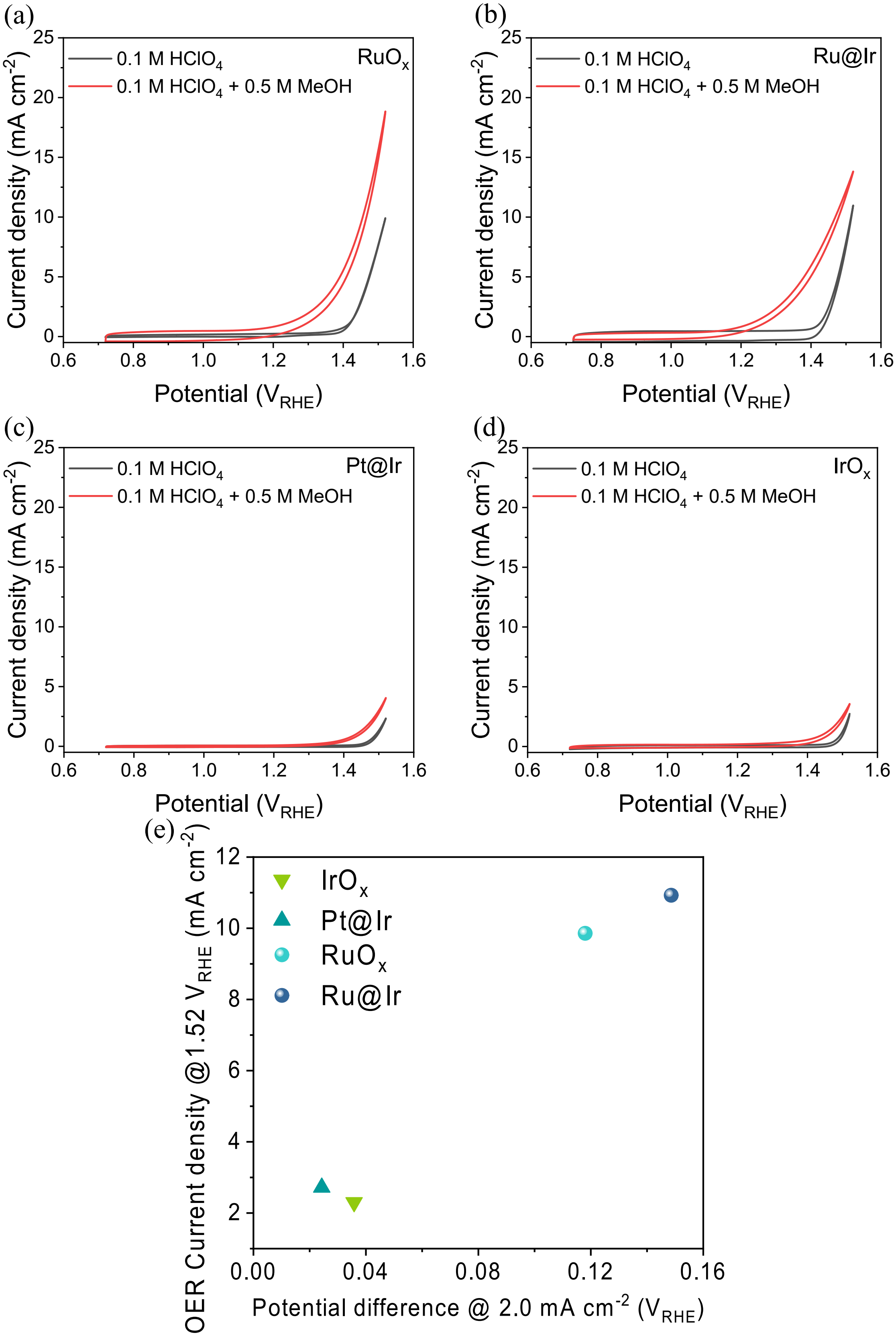
(a)
Current density (mA cm-2)
Potential (VRHE)
0.1 M HClO4
0.1 M HClO4 + 0.5 M MeOH
RuOx
0
5
10
15
20
25
0.6
0.8
1.0
1.2
1.4
1.6
(b)
Ru@Ir
(c)
Pt@Ir
(d)
IrOx
(e)
OER Current density @1.52 VRHE (mA cm-2)
Potential difference @ 2.0 mA cm-2 (VRHE)
IrOx
Pt@Ir
RuOx
Ru@Ir
2
4
6
8
10
12
0.00
0.04
0.08
0.12
0.16

Fig. S10 CV curves of RuO_x, Ru@Ir, Pt@Ir, and IrO_x for measuring OER and methanol oxidation reaction (MOR) activities in 0.10 M $HClO_4$ and 0.10 M $HClO_4$ + 0.50 M MeOH solution within 0.72–1.52 V_{RHE} at a scan rate of 50 mV s^{-1}. CV curves of (a) RuO_x, (b) Ru@Ir, (c) Pt@Ir, and (d) IrO_x. (e) Relationship between MOR activity and OER activity, with the x-axis representing the potential difference between OER and MOR at 2.0 mA cm^{-2}, and the y-axis indicating the OER current density at 1.52 V_{RHE}.

Notably, the PEMWE device performance was not directly relevant to the intrinsic OER kinetics of the fabricated electrodes. In half-cell measurements, the electrodes containing Ru catalysts—that is, RuO_x and Ru@Ir—exhibited considerably higher OER activity than that of the Ru-free electrodes. Because Ru is oxophilic, RuO_x is considered the benchmark OER catalyst with higher activity than that of IrO_x (Fig. S9b). Additionally, it exhibits optimal binding energy with *OH and *O. In this study, Ru@Ir exhibited an even higher OER activity than that of RuO_x, owing to the synergetic effect of Ru and Ir. RuO_x produces active hydroxyl (*OH) groups on its surfaces with smaller activation energies than those of IrO_x, and facilitates many oxidation reactions, such as those of MeOH and water.[4] Although Ru@Ir exhibited lower MeOH oxidation activity than that of RuO_x, possibly owing to the reduced Ru area shielded by IrO_x in Ru@Ir, it showed higher OER activity than that of RuO_x as the facile supply of *OH by Ru surfaces accelerated the OER at Ru@Ir. However, the device performance was not genuinely influenced by the OER kinetics of the electrodes, but was more affected by other factors such as ohmic resistance and mass transport. Therefore, Ru@Ir and Pt@Ir exhibited compatible device performance metrics regardless of the different anodes used (Fig. 1g-i).

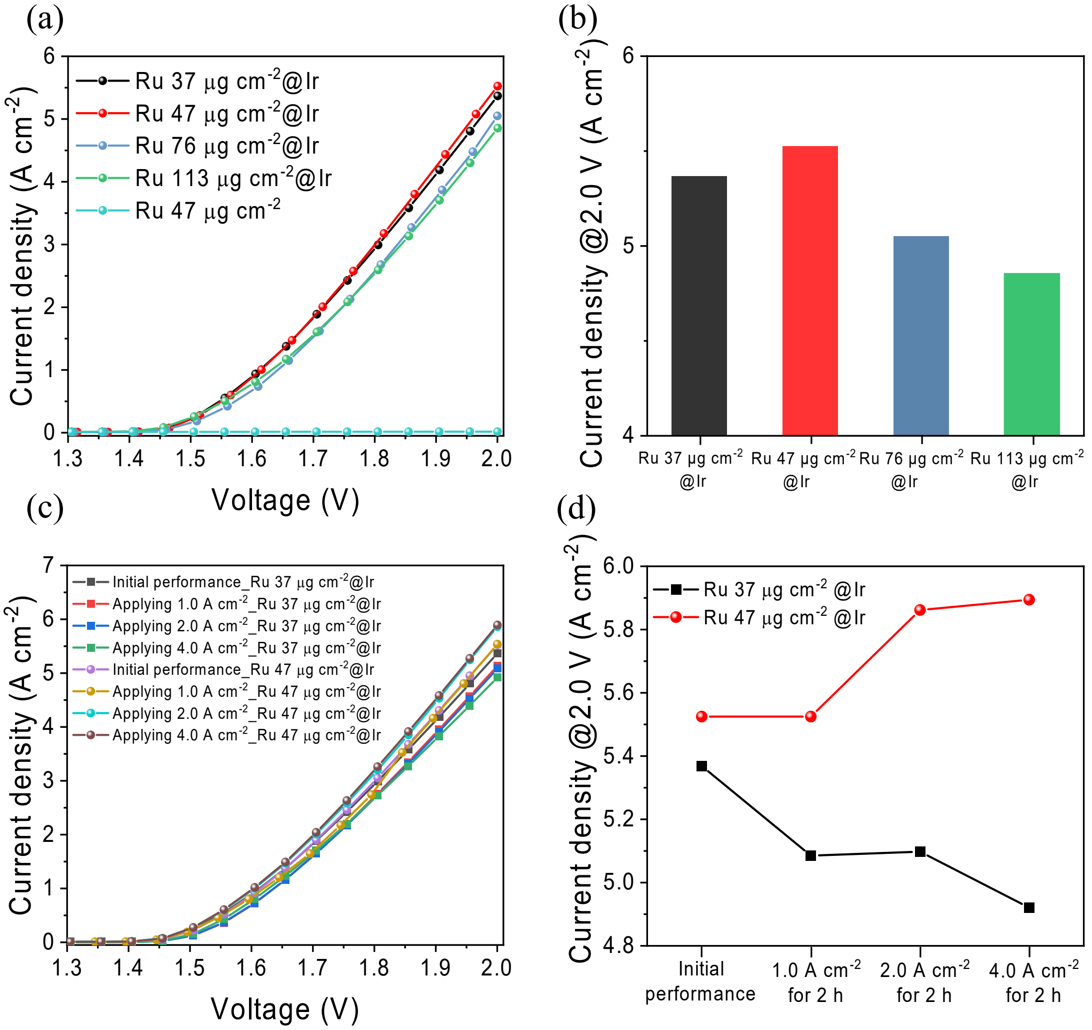

Fig. S11 Determination of optimal Ru@Ir sample. (a) LSV polarization curves and (b) current density at 2.0 V of Ru@Ir specimens obtained at various Ru deposition times (1 min [Ru 37 μg cm^{-2}], 2 min [Ru 47 μg cm^{-2}], 5 min [Ru 76 μg cm^{-2}], and 10 min [Ru 113 μg cm^{-2}]), (c) LSV polarization curves of Ru 37 μg cm^{-2}@Ir and Ru 47 μg cm^{-2}@Ir during 6 h test, and (d) change in current density of Ru 37 μg cm^{-2}@Ir and Ru 47 μg cm^{-2}@Ir after 6 h chronopotentiometry (CP) test.

The physical integrity, morphology, and water electrolysis performance of Ru@Ir were clearly affected by the deposition conditions of the Ru interlayer. The initial performance of the PEMWE devices decreased with increasing Ru deposition time or higher loading of Ru in Ru@Ir. For example, LSV curves indicated that Ru 113 µg cm^{-2}@Ir, corresponding to 10 min of Ru deposition, exhibited a 15% lower current density than that of Ru 47 µg cm^{-2}@Ir, which corresponded to 2 min of Ru deposition. SEM images (Fig. S2) suggested that the large, thick Ru@Ir films readily detached from the Ti-PTL when the Ru was deposited for longer than 5 min (76 µg cm^{-2} of Ru). Ru 47 µg cm^{-2}@Ir exhibited the highest activity and initial stability for 6 h, since Ru in Ru 47 µg cm^{-2}@Ir is firmly attached to the Ti PTL among other Ru@Ir electrodes.

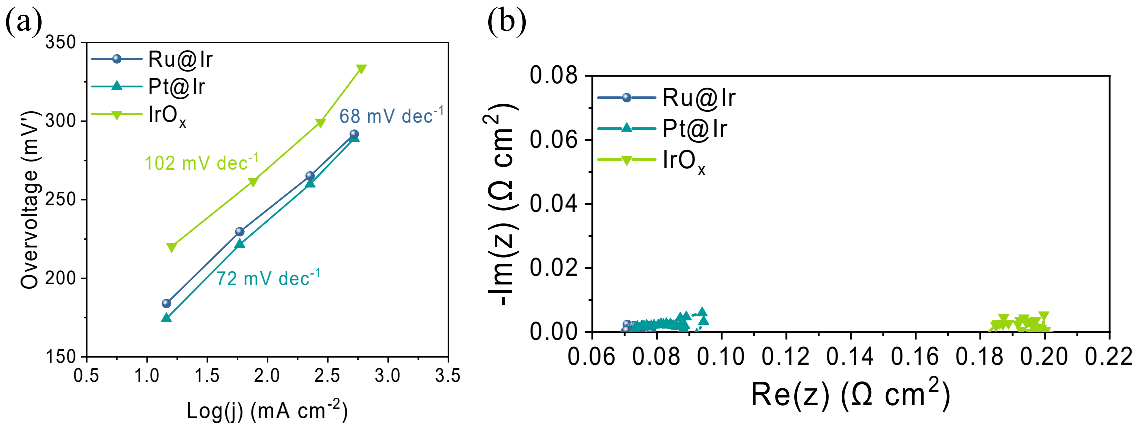

Fig. S12 (a) Tafel plots derived from LSV curves shown in Fig. 1g, and (b) Potentiostatic electrochemical impedance spectroscopy (PEIS) analysis at 2.0 V_{cell} for Ru@Ir, Pt@Ir, and IrO_x.

The method used to decompose the total overvoltage into ohmic, kinetic, and mass transfer components is as follows. The ohmic resistance is firstly obtained from electrochemical impedance spectroscopy (EIS) measurements (Fig. S12b). The ohmic overvoltage is then calculated by multiplying the ohmic resistance by the current density (1.0 A cm^{-2} in this study). The kinetic overvoltage is determined based on Fig. S12a, where the x-axis represents log(j) and the y-axis shows the ohmic resistance-compensated overvoltage (η'). This compensated overvoltage is obtained by subtracting the theoretical potential (1.23 V) from the measured cell voltage. The resulting plot follows the Tafel equation: $\eta' = a + b \cdot \log(j)$, where η' is the kinetic overvoltage, a is the y-intercept, and b is the Tafel slope. By substituting j = 1.0 A cm^{-2}, the kinetic overvoltage at the target current density, i.e. 1.0 A cm^{-2}, is calculated. Finally, the mass transfer overvoltage is determined by subtracting the sum of the ohmic and kinetic overvoltages from the total overvoltage measured at 1.0 A cm^{-2}.

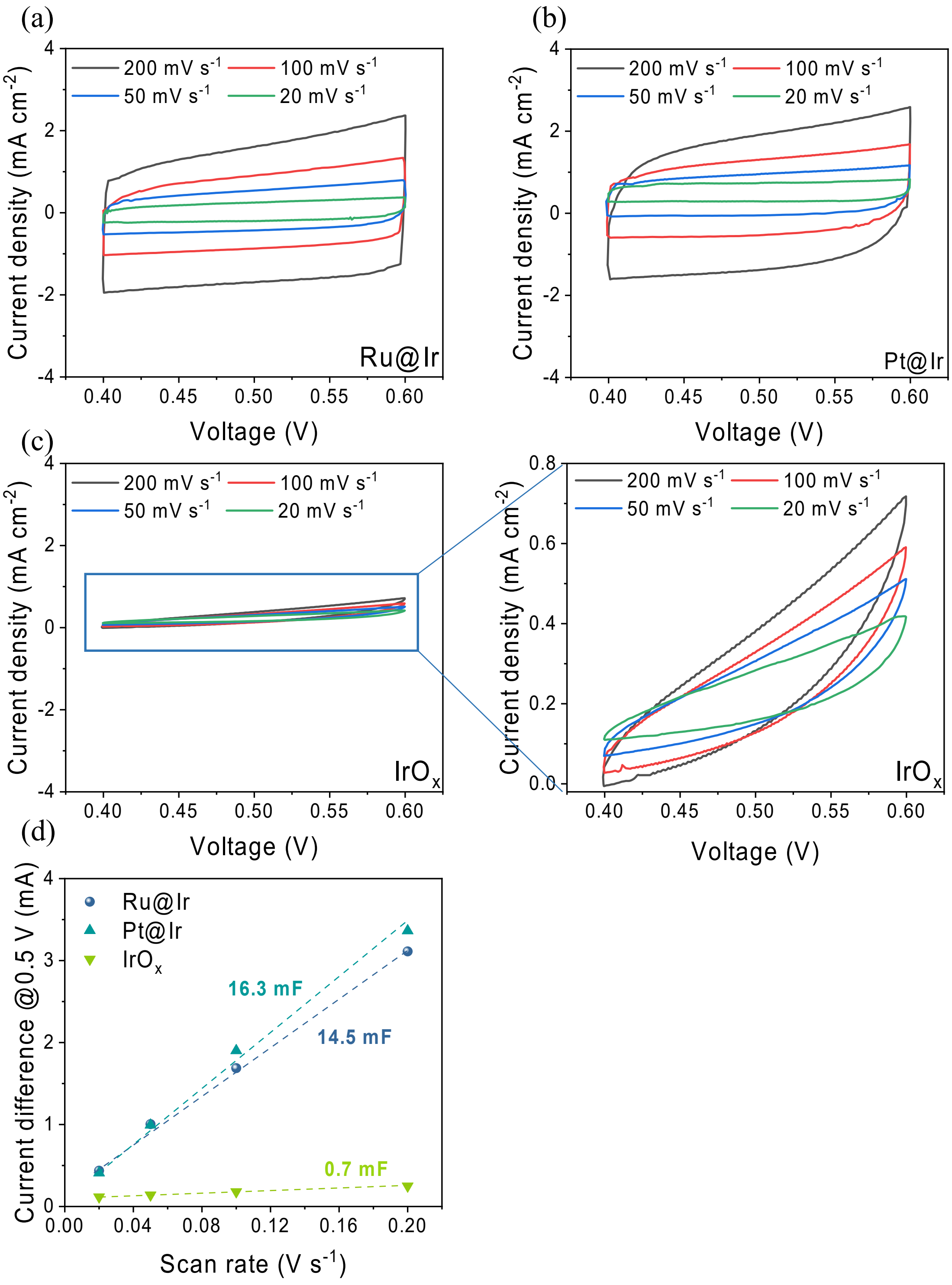

Fig. S13 CV curves obtained from 0.40 to 0.60 V (vs. pseudo-RHE) at scan rates of 20–200 mV

s^{-1} for (a) Ru@Ir, (b) Pt@Ir, and (c) IrO_x after 1 h of water electrolysis (WE) for comparing C_{dl}. (d) Linear plots of capacitive current against scan rate.

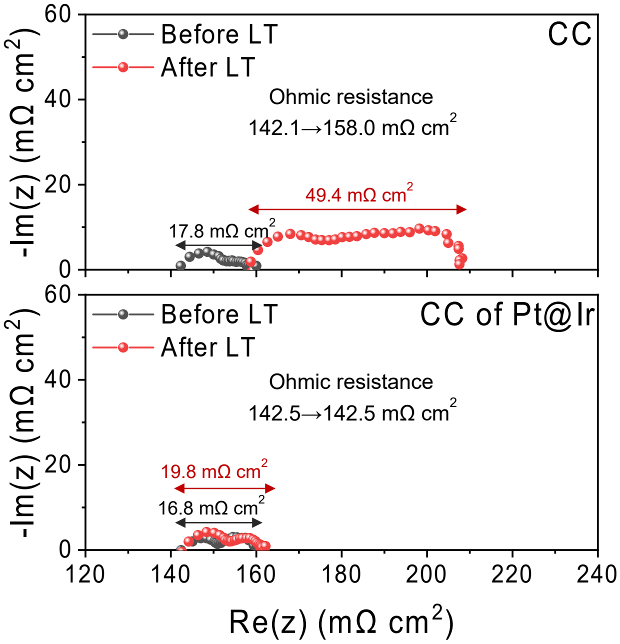

Fig. S14 Galvanostatic electrochemical impedance spectroscopy (GEIS) analysis at 2.0 A cm^{-2} for Ru@Ir and Pt@Ir subjected to CC operation before and after LT.

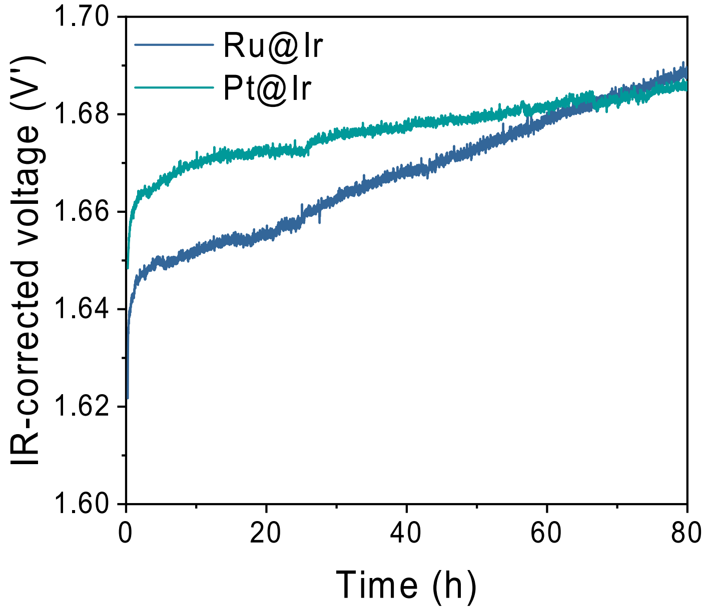

Fig. S15 IR-corrected CP curves of Ru@Ir and Pt@Ir in CC operation for calculating rate of degradation induced by catalyst deterioration.

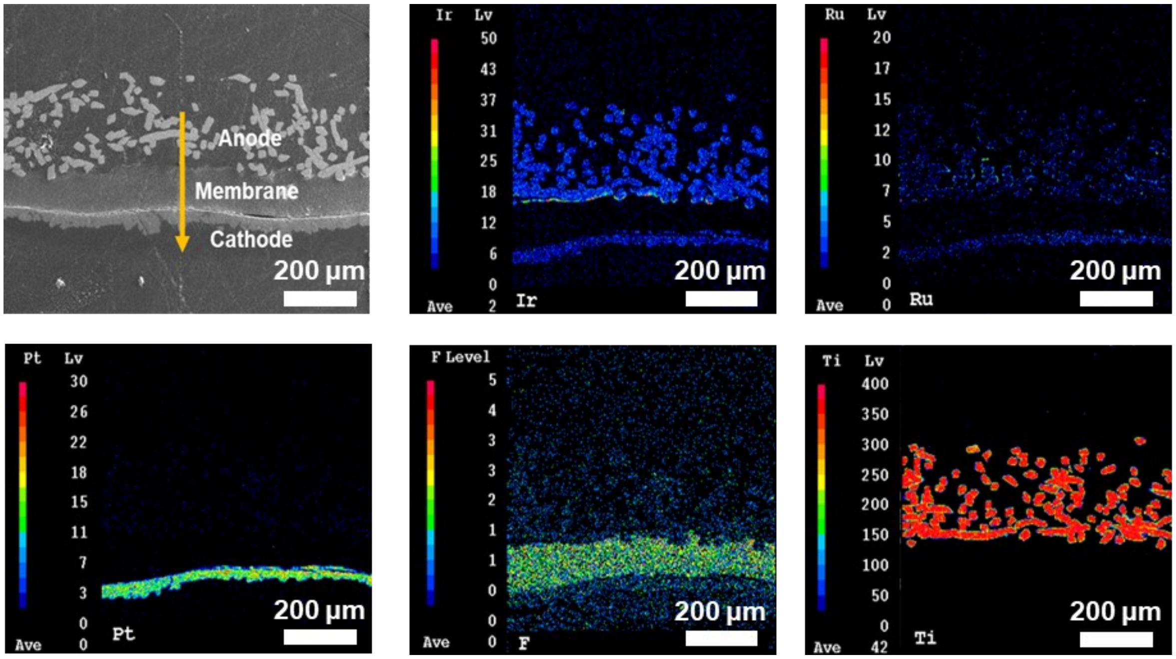

Fig. S16 Secondary electron (SE) image of MEA and corresponding elemental mapping images of Ti, Ir, Ru, F, and Pt. Data were obtained by electron probe microanalysis (EPMA) of MEA with Ru@Ir after CC operation.

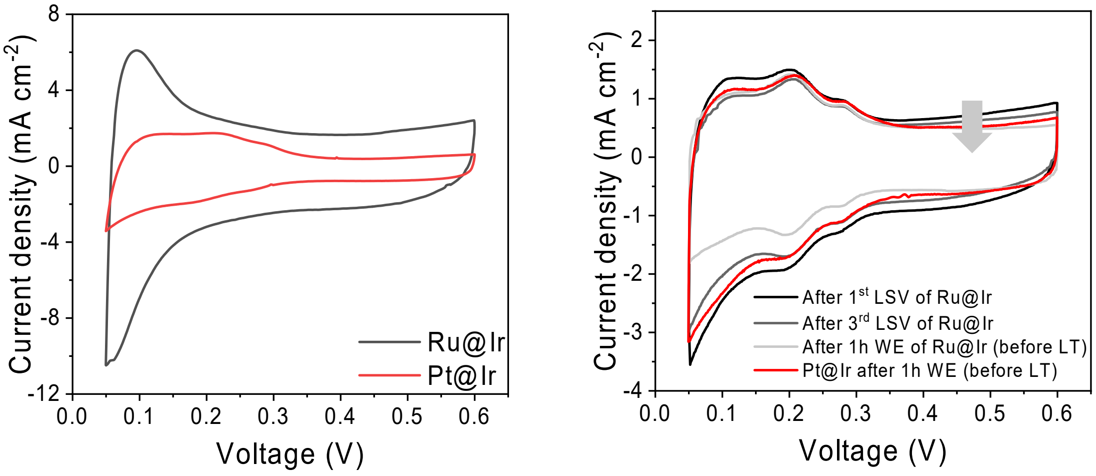

Fig. S17 CV curves of Ru@Ir and Pt@Ir for calculating ECSA from H_{upd} measured within the 0.05–0.60 V range at a scan rate of 50 mV s^{-1}. (a) fresh samples and (b) samples after 1 h of WE.

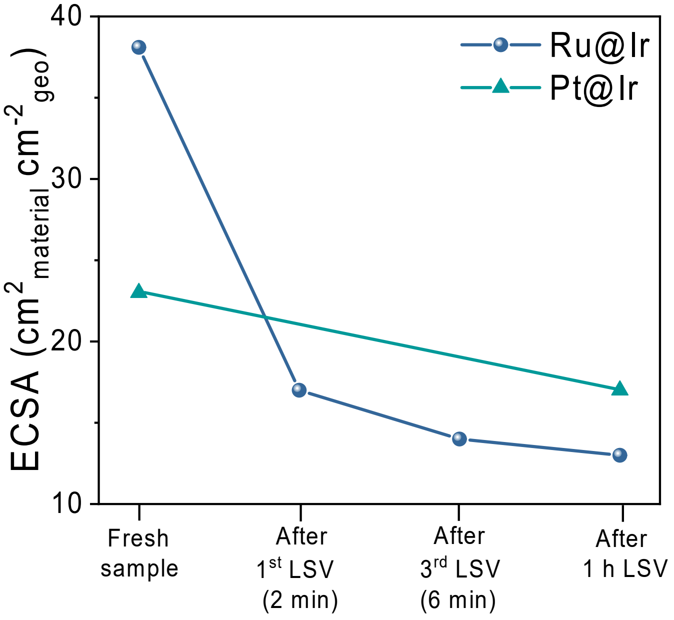

Fig. S18 ECSA estimated from H_{upd} variation for Ru@Ir and Pt@Ir during 1 h of WE.

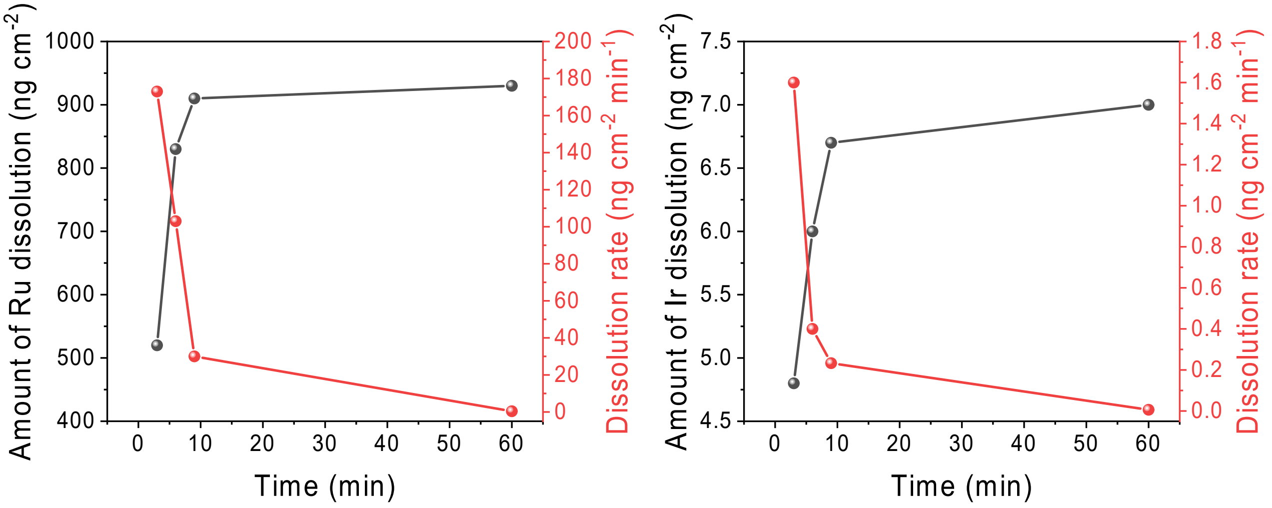

Fig. S19 ICP-MS results for Ru and Ir dissolution during 1 h of WE. These experiments were conducted by applying 2.0 A cm^{-2}.

The cumulative amount of Ru dissolution was measured as 520, 830, 910, and 930 ng_{Ru} cm^{-2} after 3, 6, 9, and 60 min of OER, respectively. Since the majority of Ru dissolution occurred within the first 6 min, the corresponding dissolution rate was calculated as 173, 103, 30, and 0.39 ng_{Ru} cm^{-2} min^{-1}. Despite a 64% reduction in the H_{upd} area observed in the CV curves after just 6 min of OER (Fig. S17), the amount of Ru detected outside the reactor accounted for only ~2% of the total Ru loading (44.7 μg_{Ru} cm^{-2}). This discrepancy may be attributed to the adsorption of dissolved Ru onto internal cell components or tubing, or to the limited dissolution of Ru protected beneath the Ir overlayer during the 1 h operation. In contrast, the cumulative amount of dissolved Ir was only ~0.1% of that of Ru, although it exhibited a similar dissolution trend, with measured values of 4.8, 6.2, 6.7, and 7 ng_{Ir} cm^{-2} at 3, 6, 9, and 60 min, respectively. The corresponding Ir dissolution rate was 1.6, 0.4, 0.233, and 0.00588 ng_{Ir} cm^{-2} min^{-1}.

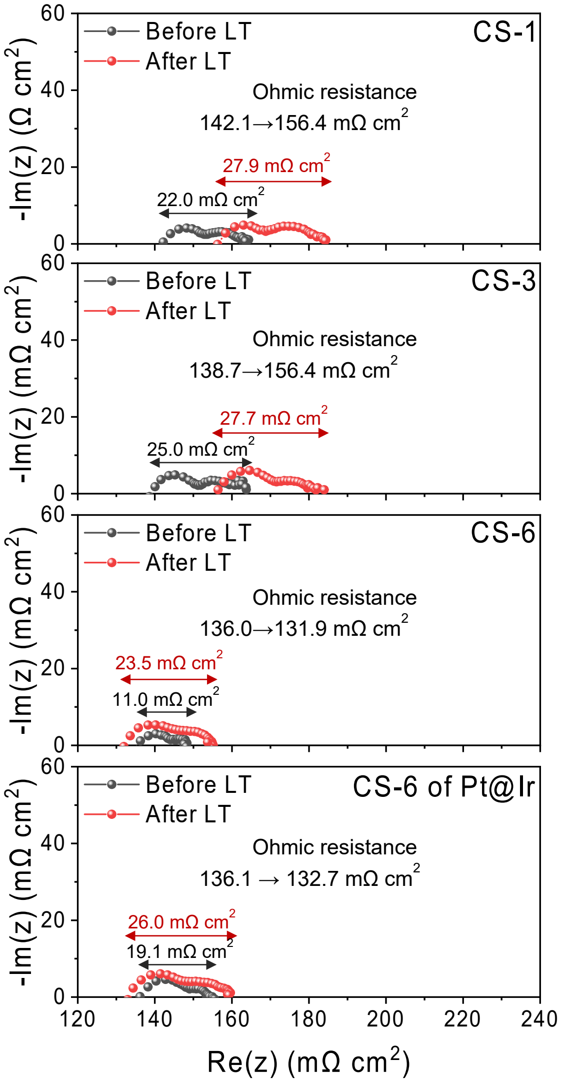

Fig. S20 GEIS analysis at 2.0 A cm^{-2} for Ru@Ir subjected to CS-1, CS-3, and CS-6 operations, as well as Pt@Ir subjected to CS-6 operation before and after LT.

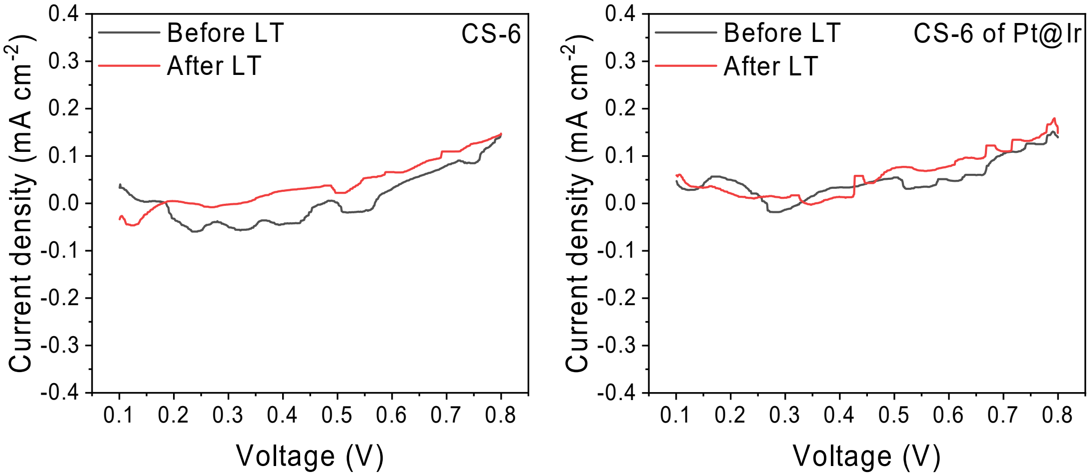

Fig. S21 LSV curves for measuring H_2 crossover to assess membrane status before and after LT.

Given that the hydrogen crossover current remained similar before and after LT under CS-6 operation in both Ru@Ir and Pt@Ir, the observed reduction in ohmic resistance after LT cannot be attributed to membrane thinning. Instead, the decrease in ohmic resistance during CS-6 operation is likely due to enhanced electrode–membrane contact, which was improved through prolonged exposure to high operating temperatures, without inducing significant oxidation of the catalyst or Ti-PTL (Fig. 4c–e).

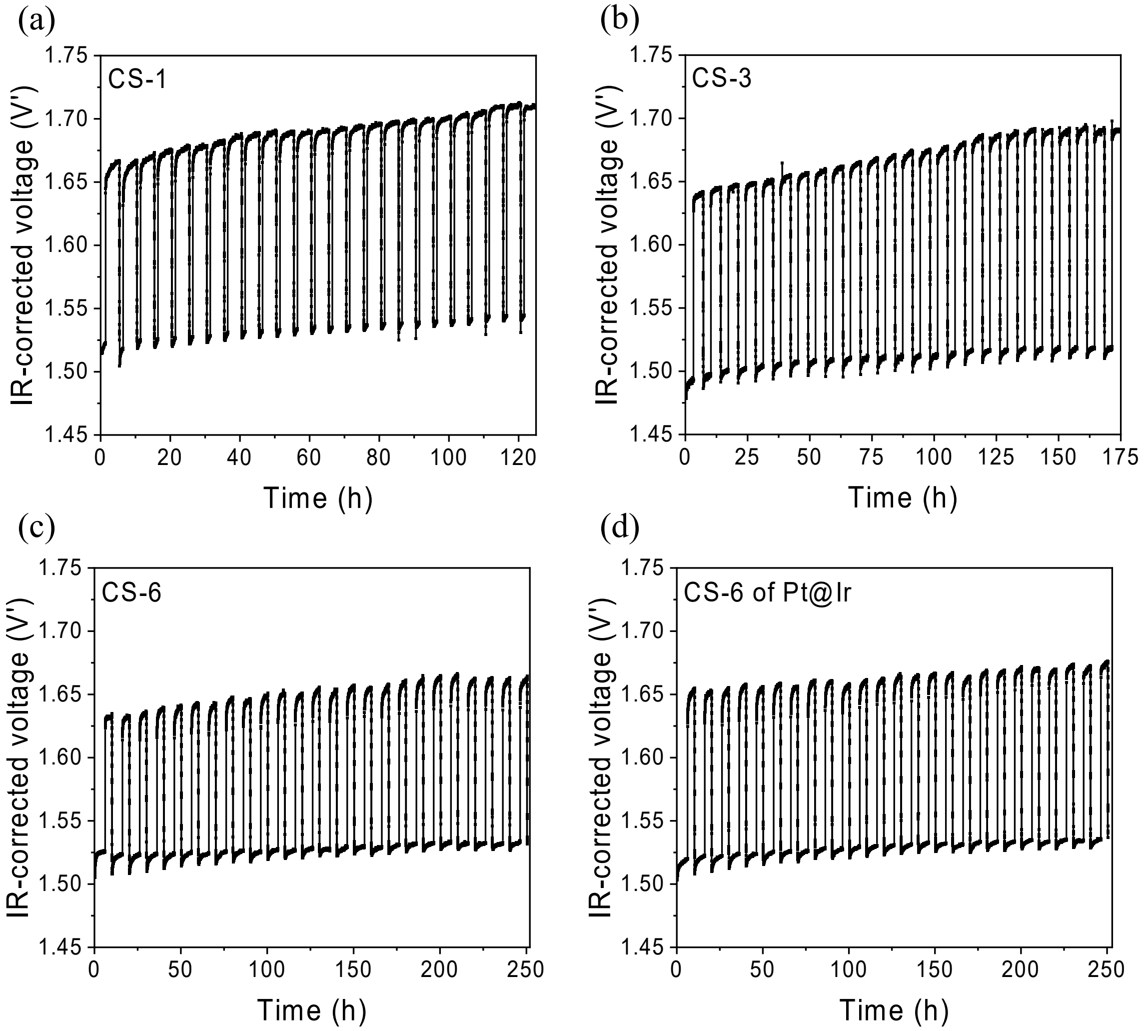

Fig. S22 IR-corrected CP curves of Ru@Ir subjected to (a) CS-1, (b) CS-3, and (c) CS-6 operations, and that of (d) Pt@Ir subjected to CS-6 operation, for calculating degradation rate from catalyst degradation.

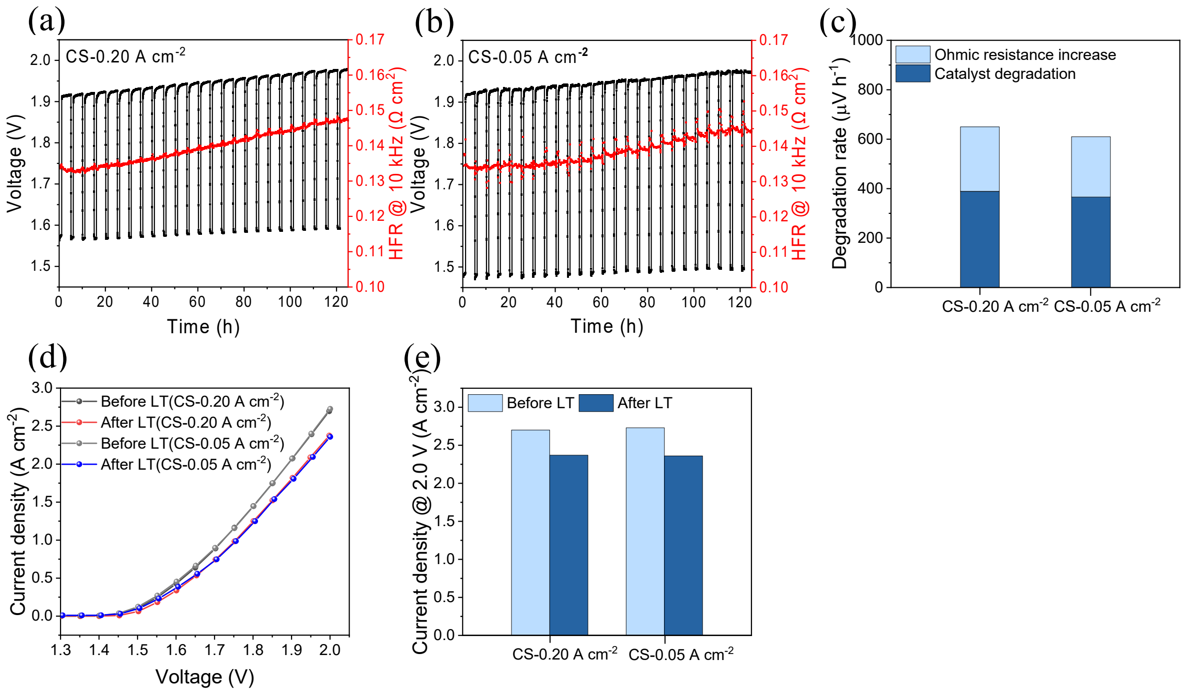

Fig. S23 Long-term durability testing (LT) of Ru@Ir to confirm low-applied-voltage effects, with 2.0 A cm^{-2} applied in the HCO, and 0.20 and 0.05 A cm^{-2} applied in the LCO. Both operations were performed under the same conditions as those of CS-1, except for current density. CP curves for (a) CS-0.20 A cm^{-2} and (b) CS-0.05 A cm^{-2}, (c) Degradation rate calculated from CP curves during HCO, (d) LSV polarization curves before and after LT, and (e) current density at 2.0 V.

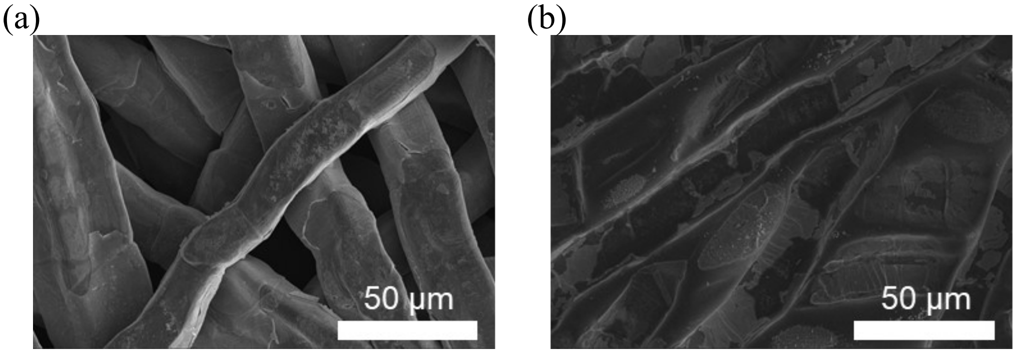

Fig. S24 SEM images of Ru@Ir detached from MEA after LT. (a) Ti-PTL side and (b) membrane side.

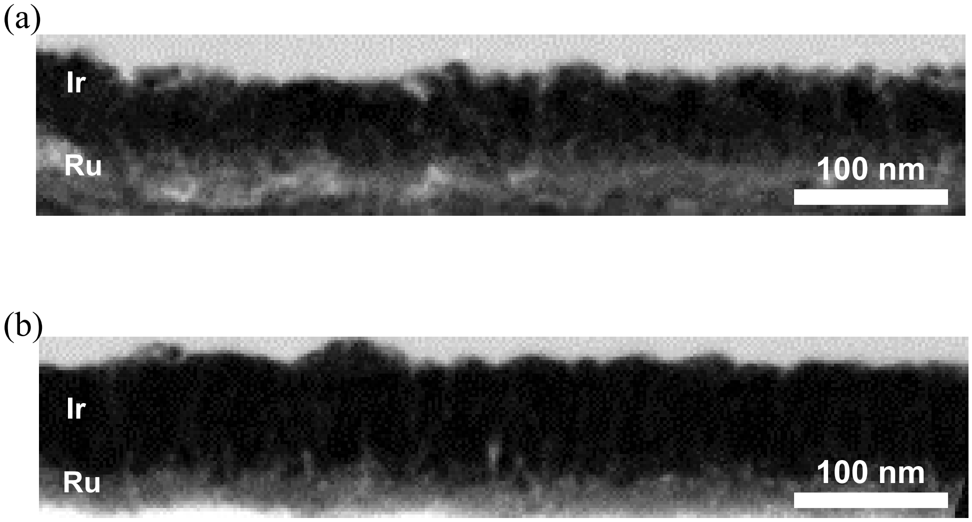

Fig. S25 Cross-sectional STEM images of Ru@Ir after (a) CC and (b) CS-6 operations.

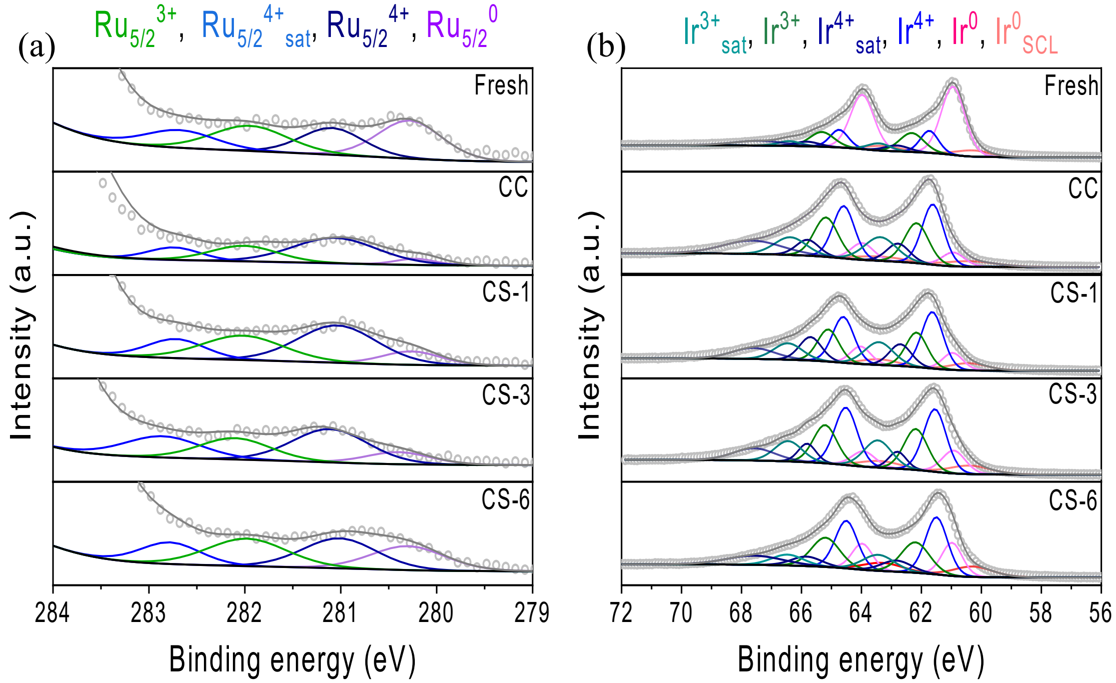

Fig. S26 (a) Ru $3d_{5/2}$ and (b) Ir 4f XPS spectra of Ru@Ir on the Ti-PTL side.

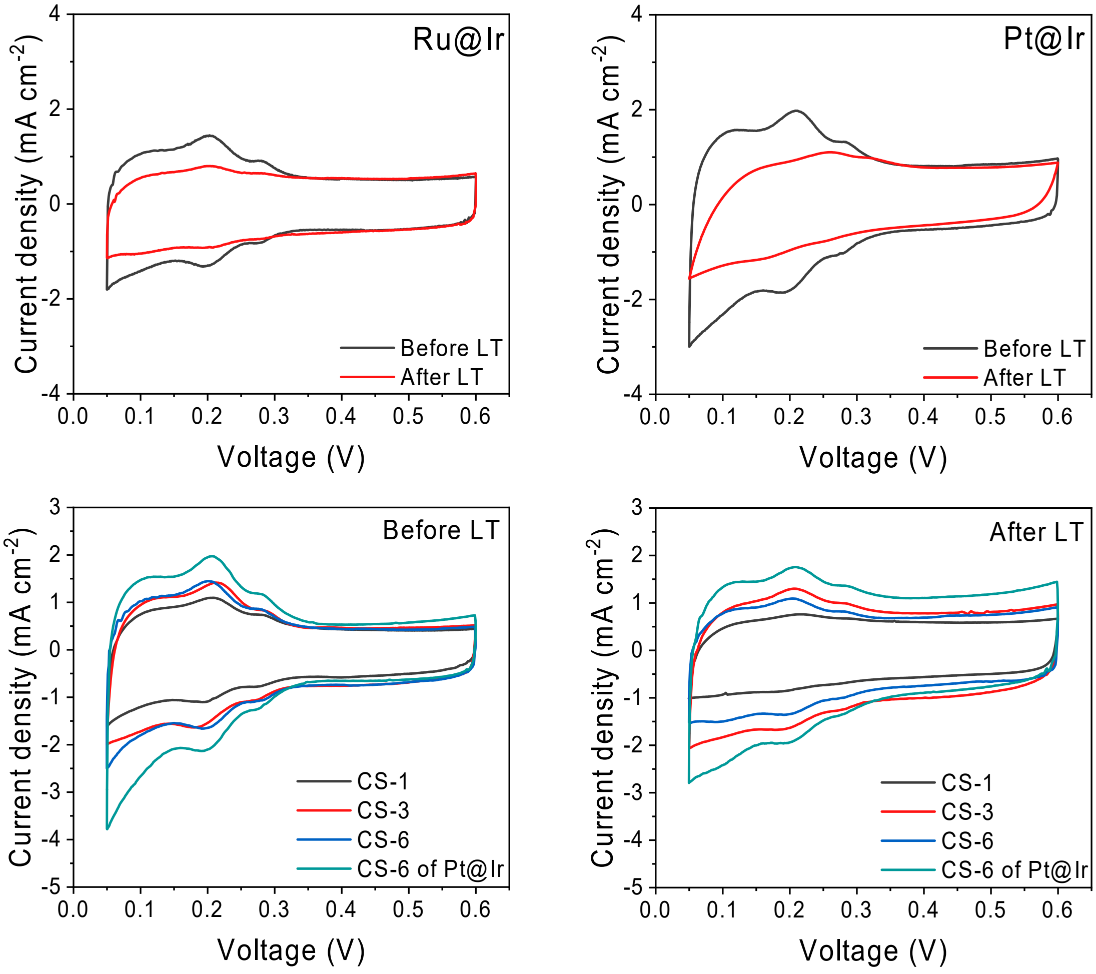

Fig. S27 CV curves for estimating ECSA from H_{upd} measured within the 0.05–0.60 V range (vs. pseudo- RHE) at a scan rate of 50 mV s^{-1}. (a) Ru@Ir and (b) Pt@Ir before and after CC operation. Ru@Ir subjected to CS-1, CS-3, and CS-6 operations, and Pt@Ir subjected to CS-6 operation (c) before and (d) after durability tests.

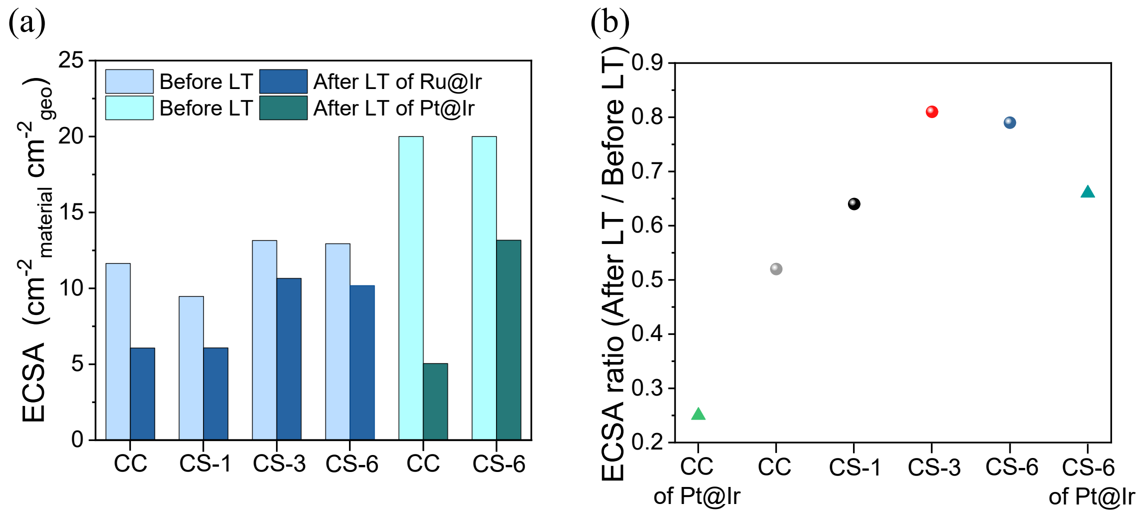

Fig. S28 (a) ECSA determined from variation in H_{upd} for Ru@Ir and Pt@Ir before and after durability tests, and (b) ECSA ratio estimated from H_{upd} for evaluating residual metallic Ir by dividing the ECSA values obtained after and before the tests. The ECSA derived from H_{upd} after LT represented the residual metallic Ir, as all catalysts exhibited a larger surface area after LT than that before LT (Fig. S25-S28).

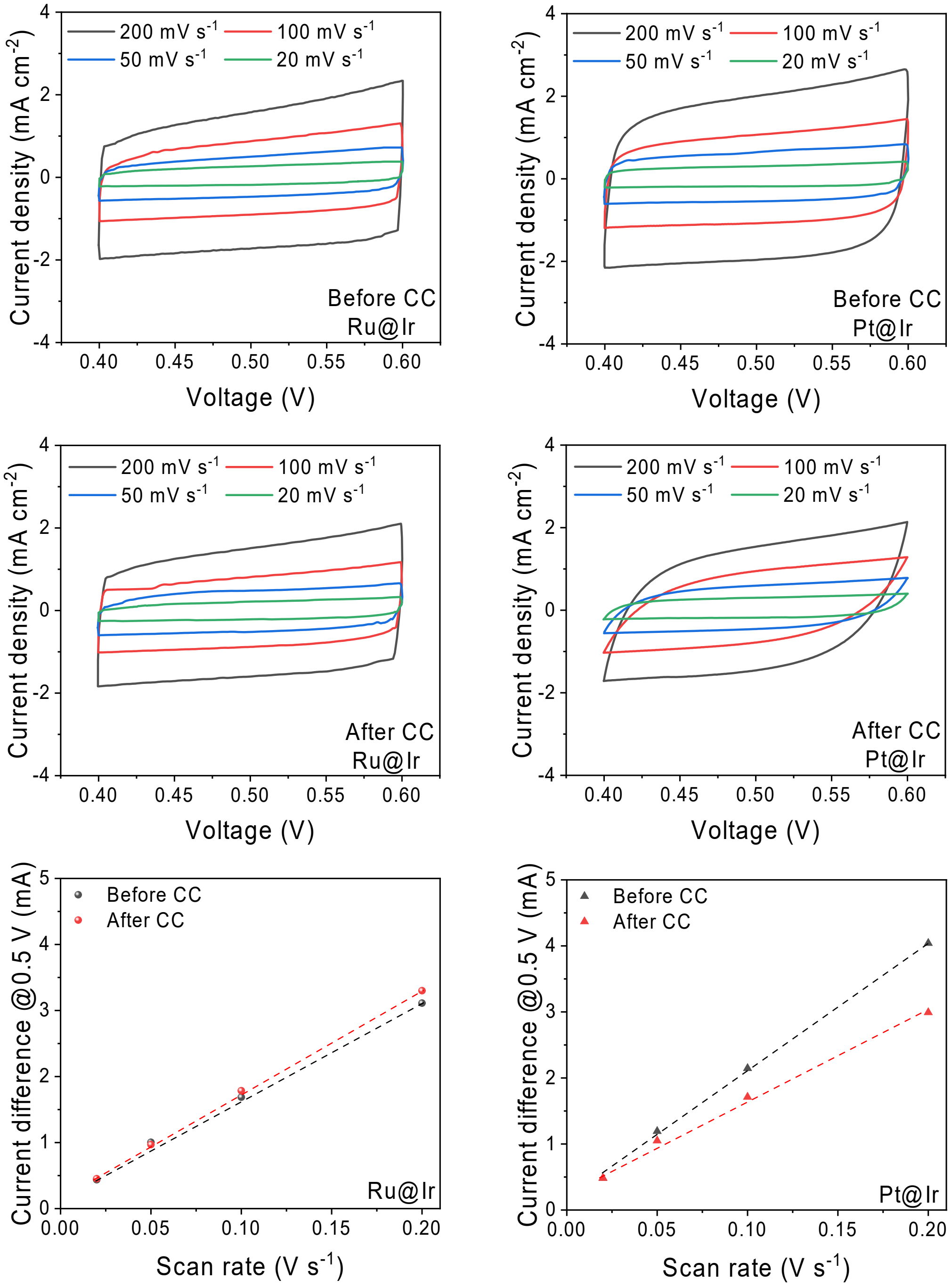

Fig. S29 CV curves of Ru@Ir and Pt@Ir in the 0.40–0.60 V range (vs. pseudo- RHE) at scan rates ranging from 20 to 200 mV s^{-1} in CC operation.

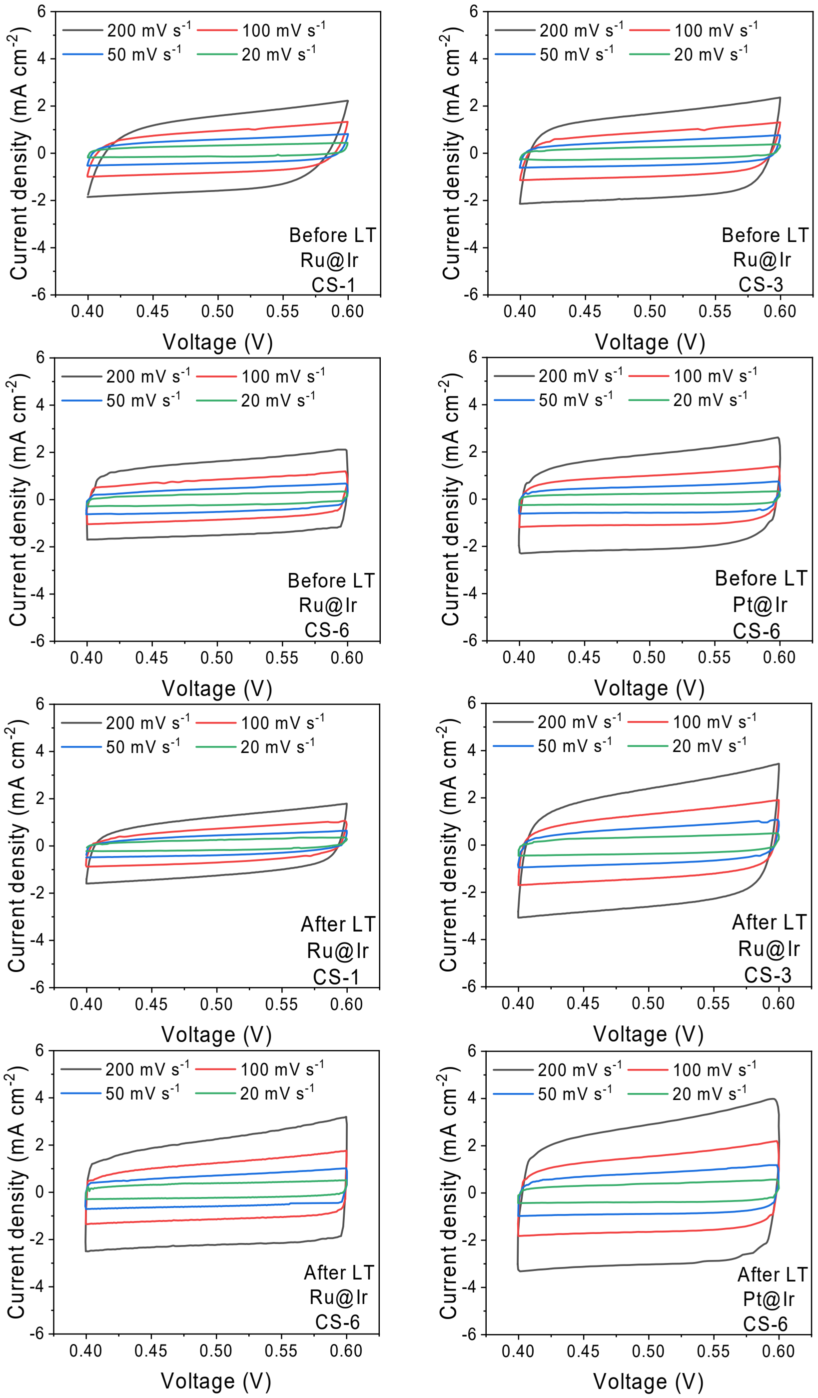

Fig. S30 CV curves of Ru@Ir and Pt@Ir in the 0.40–0.60 V range (vs. pseudo-RHE) at scan rates ranging from 20 to 200 mV s^{-1} in CS operation.

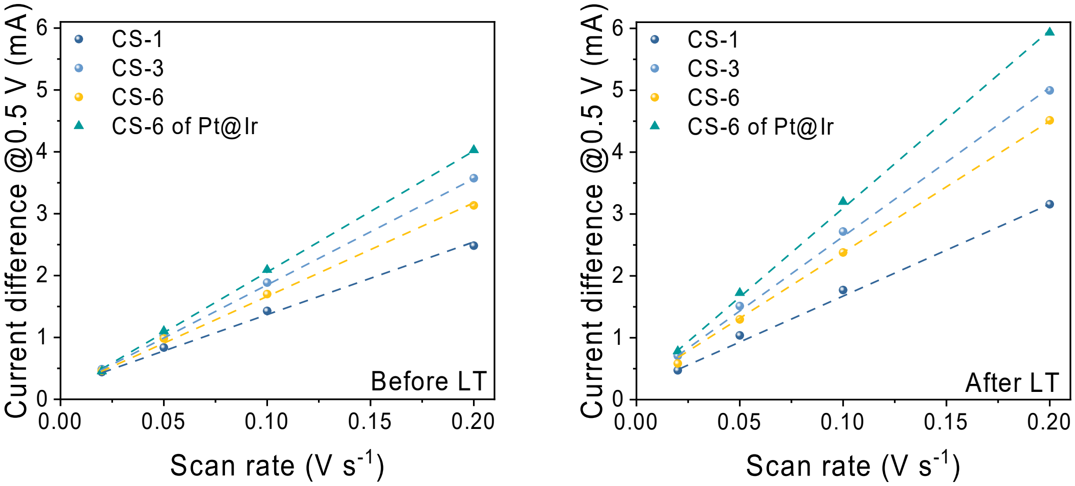

Fig. S31 Linear plots of capacitive current against scan rate in CS operation.

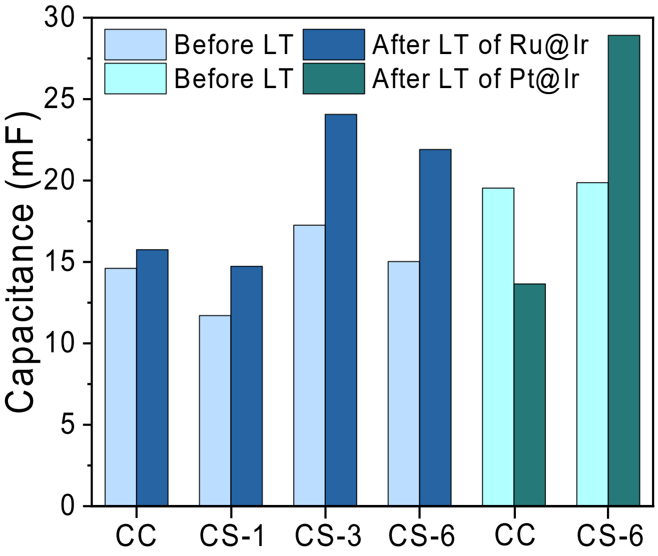

Fig. S32 Capacitance variation of Ru@Ir and Pt@Ir before and after LT.

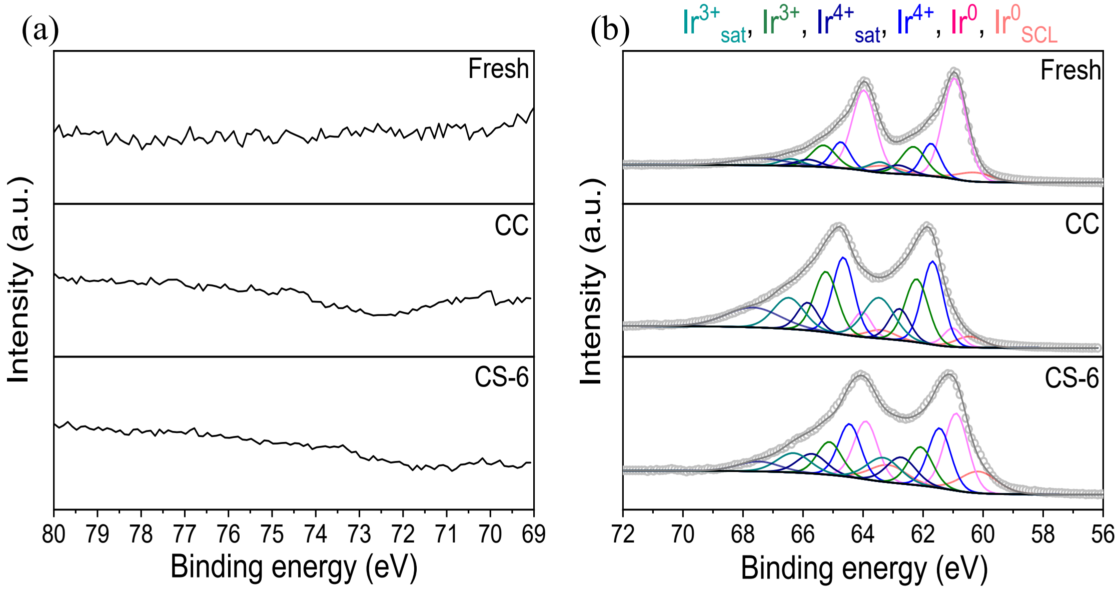

Fig. S33 (a) Pt 4f and (b) Ir 4f XPS spectra of Pt@Ir on Ti-PTL side.

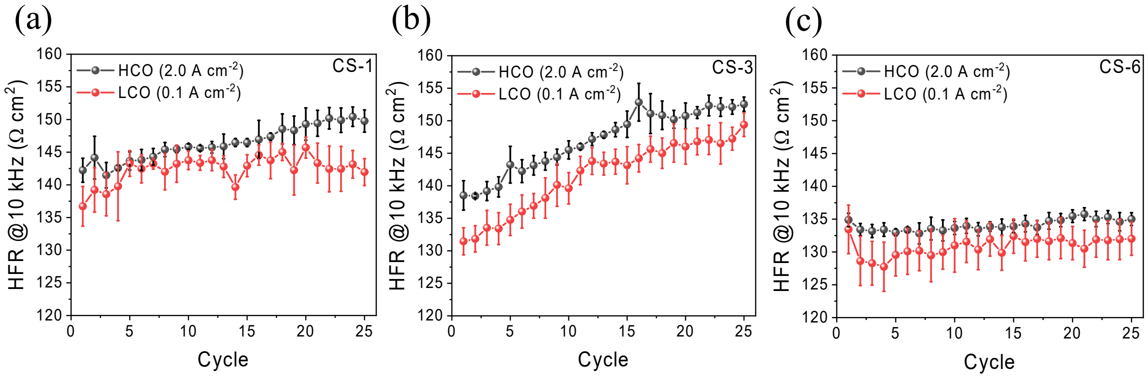

Fig. S34 HFR of Ru@Ir at 10 kHz during CS operation. (a) CS-1, (b) CS-3, and (c) CS-6. The HFR of HCO was higher than that of LCO in all cases, indicating that bubbles diffused out during LCO.

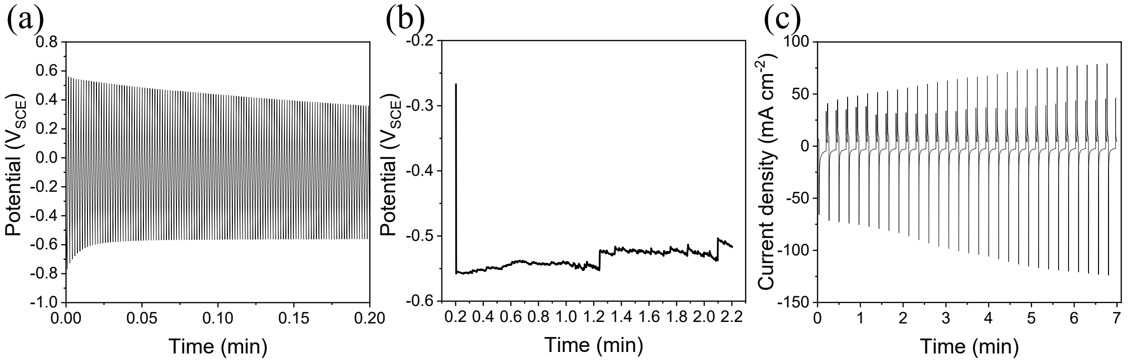

Fig. S35 CP and CA curves of Ru@Ir during electrodeposition for preparing the electrode for the model study. The Ru deposition method was changed to exclude the effects of the laminated morphology. (a) CA curve of pre-cycling during Ru deposition (-30 mA cm^{-2} and 25 mA cm^{-2} were applied in turn 120 times), (b) CA curve of Ru deposition (applying -30 mA cm^{-2} for 2 min), and (c) CA curve of Ir deposition.

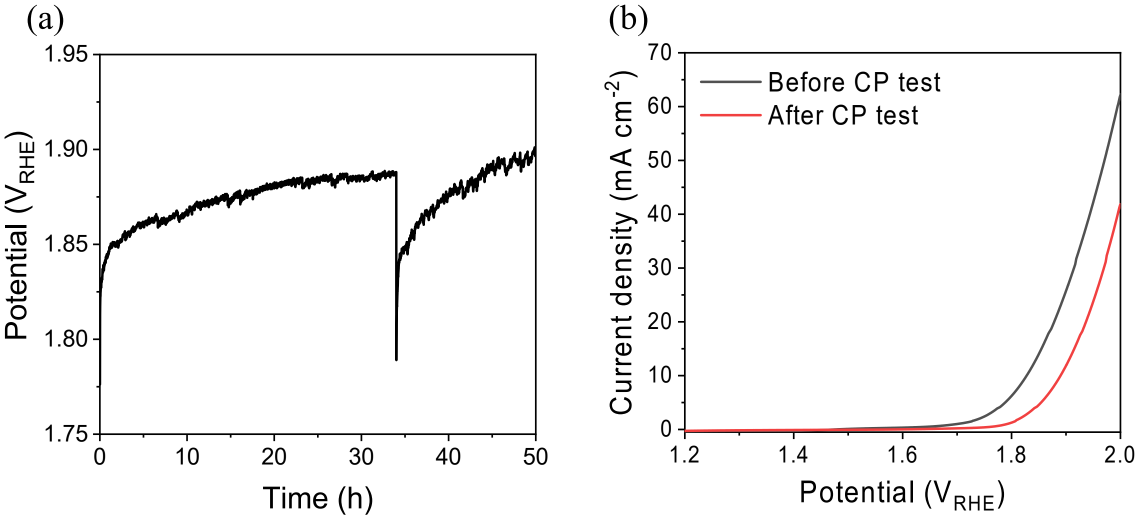

Fig. S36 (a) CP curves acquired at a constant current of 5 mA cm^{-2} for 50 h, and (b) LSV polarization curves of Ru@Ir before and after tests conducted at a scan rate of 50 mV s^{-1}. This experiment was conducted in a 0.5 M Na_2SO_4 solution.

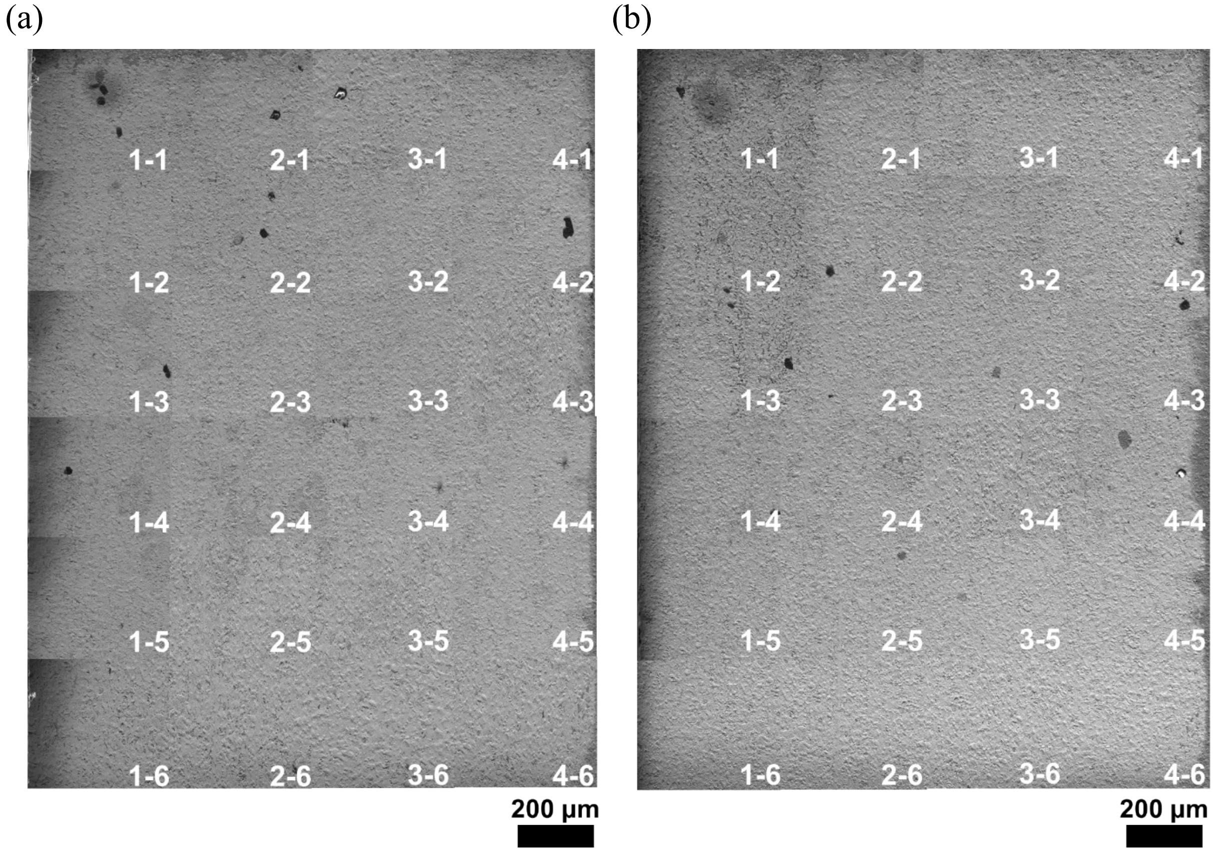

Fig. S37 SEM image of Ru@Ir on Ti foil obtained (a) before and (b) after model study.

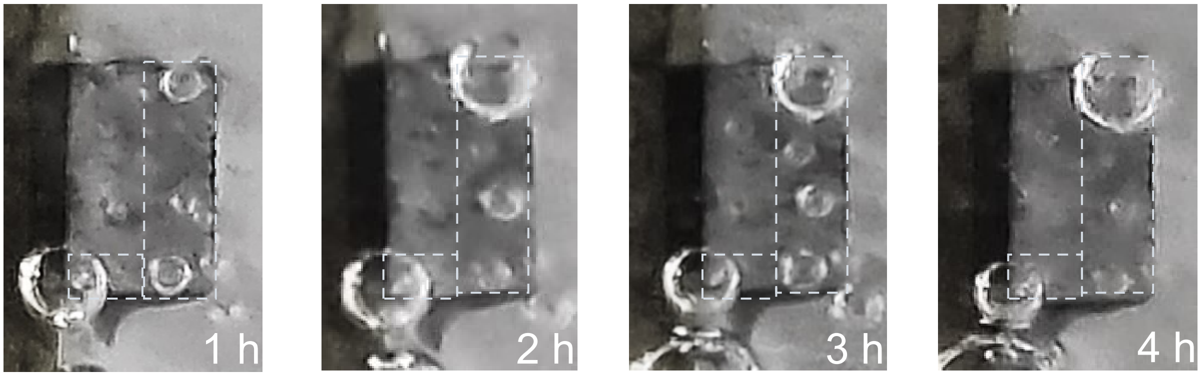

Fig. S38 Images of Ru@Ir electrode after 1, 2, 3, and 4 h of CP tests. (Dashed lines show areas where bubbles commonly existed during the CP test.)

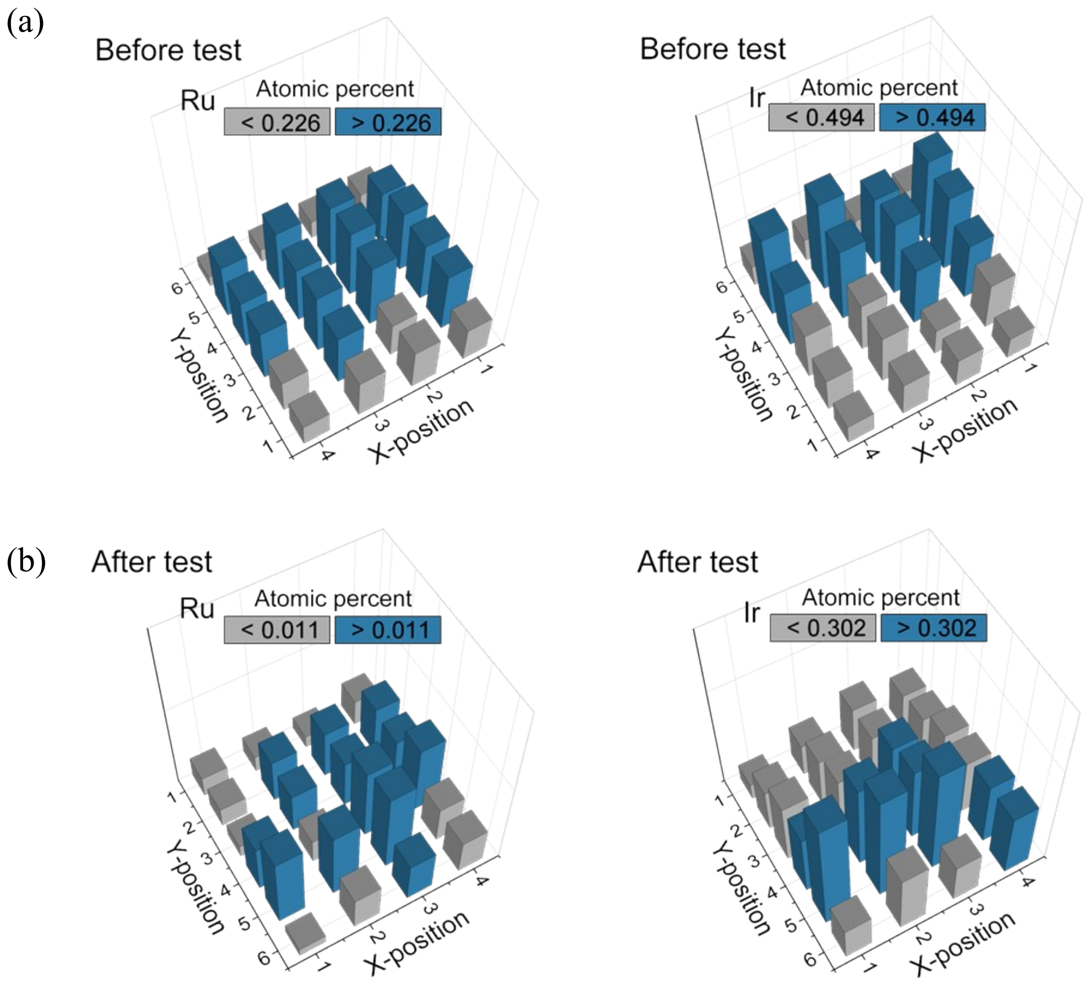

Fig. S39 3D bar graphs obtained (a) before and (b) after the tests. Data show atomic percentages of Ru and Ir in the compartmented matrix, normalized by the sum of Ti and O.

Table S1. ICP-OES results of the synthesized catalysts.

Sample	**Ir** **(µg cm^{-2})**	**Ti protector** **(µg cm^{-2})**	**Total** **(µg cm^{-2})**
Ru 1 min	N/A	37.2	37.2
Ru 2 min	N/A	47.1	47.8
Ru 5 min	N/A	76.3	76.3
Ru 10 min	N/A	87.8	87.8
Ru 1 min@Ir	46.9	31.0	77.9
Ru 2 min@Ir	60.7	44.7	105.4
Ru 5min@Ir	48.2	64.8	113.0
Ru 10min@Ir	66.2	113.0	179.2
Ir on bare Ti	<30 ppm	N/A	<30 ppm
Pt@Ir	77.0	378	455.0

Supplementary References

S1. Cox, D. F., Hoflund, G. B. & Laitinen, H. A. XPS investigation of tin oxide supported platinum. *Langmuir,* 1985, **1**, 269-273. 10.1021/la00063a001.

S2. Morgan, D. J. Resolving ruthenium: XPS studies of common ruthenium materials. *Surf. Interface Anal,* 2015, **47**, 1072-1079. 10.1002/sia.5852.

S3. Pfeifer, V. et al. The electronic structure of iridium and its oxides. *Surf. Interface Anal.,* 2015*,* **48**, 261-273. 10.1002/sia.5895.

S4. Tao, H. B. et al. A general method to probe oxygen evolution intermediates at operating conditions. *Joule*, 2019, **3**, 1498-1509. 10.1016/j.joule.2019.03.012.